The Astrophysical Journal Supplement Series, 250:29 (22pp), 2020 October https://doi.org/10.3847/1538-4365/abb139

Search for Nearby Earth Analogs .III. Detection of 10 New Planets, 3 Planet Candidates, and Confirmation of 3 Planets around 11 Nearby M Dwarfs

Fabo Feng[1], Stephen A. Shectman[2], Matthew S. Clement[1], Steven S. Vogt[3], Mikko Tuomi[4], Johanna K. Teske[1,2,7], Jennifer Burt[5], Jeffrey D. Crane[2], Bradford Holden[3], Sharon Xuesong Wang[2], Ian B. Thompson[2], Matías R. Díaz[2,6], and R. Paul Butler[1]

[1] Earth and Planets Laboratory, Carnegie Institution for Science, Washington, DC 20015, USA; fengfabo@gmail.com
[2] Observatories of the Carnegie Institution for Science, 813 Santa Barbara Street, Pasadena, CA 91101, USA
[3] UCO/Lick Observatory, University of California, Santa Cruz, CA 95064, USA
[4] Centre for Astrophysics Research, University of Hertfordshire, College Lane, AL10 9AB, Hatfield, UK
[5] Jet Propulsion Laboratory, California Institute of Technology, 4800 Oak Grove Drive, Pasadena CA 91109, USA
[6] Departamento de Astronomía, Universidad de Chile, Camino El Observatorio 1515, Las Condes, Santiago, Chile
Received 2020 June 29; revised 2020 August 7; accepted 2020 August 18; published 2020 October 1

Abstract

Earth-sized planets in the habitable zones of M dwarfs are good candidates for the study of habitability and detection of biosignatures. To search for these planets, we analyze all available radial velocity data and apply four signal detection criteria to select the optimal candidates. We find 10 strong candidates satisfying these criteria and three weak candidates showing inconsistency over time due to data samplings. We also confirm three previous planet candidates and improve their orbital solutions through combined analyses of updated data sets. Among the strong planet candidates, HIP 38594 b is a temperate super-Earth with a mass of $8.2 \pm 1.7\,M_{\oplus}$ and an orbital period of 60.7 ± 0.1 days, orbiting around an early-type M dwarf. Early-type M dwarfs are less active and thus are better hosts for habitable planets than mid-type and late-type M dwarfs. Moreover, we report the detection of five two-planet systems, including two systems made up of a warm or cold Neptune and a cold Jupiter, consistent with a positive correlation between these two types of planets. We also detect three temperate Neptunes, four cold Neptunes, and four cold Jupiters, contributing to a rarely explored planet population. Due to their proximity to the Sun, these planets on wide orbits are appropriate targets for direct imaging by future facilities such as the Habitable Exoplanet Observatory and the Extremely Large Telescope.

Unified Astronomy Thesaurus concepts: Exoplanet astronomy (486); Radial velocity (1332); Exoplanet detection methods (489); M dwarf stars (982); Astrostatistics (1882); High resolution spectroscopy (2138)

Supporting material: machine-readable table

1. Introduction

One of the fundamental questions to humanity is whether there are other habitable worlds like the Earth. Since Earth is the only planet known to host life, we imagine that the best candidates for habitable worlds are Earth-sized planets around Sun-like stars (though there is currently no data to confirm this bias). However, the Earth only induces $0.09\ \mathrm{m\ s^{-1}}$ radial velocity (RV) variation on the Sun and ∼84 parts per million (ppm) transit depth. Signals with such a small transit and such as long period are beyond the capabilities of any existing advanced instrument/telescope. Modern facilities are sensitive to Earth-sized planets around low-mass stars (so-called Earth analogs) such as M dwarfs. Although M dwarfs are more active than Sun-like stars and the planets in their habitable zones (HZs; Kopparapu et al. 2014) presumably evolved to possess tidally locked synchronous orbits, there are plausible mechanisms to reduce the harm caused by stellar flaring and tidal locking (Tarter et al. 2007; Shields et al. 2016). As ∼70% of the stars in our Galaxy are M dwarfs according to the REsearch Consortium On Nearby Stars (RECON) sample of nearest stars,[8] the Earth-sized planets around these low-mass stars provide an important sample for habitability studies and biosignature searches.

On the other hand, because early-type M dwarfs are less active than mid-type and late-type M dwarfs (Mohanty & Basri 2003; West et al. 2015), an HZ planet would require a weaker magnetic field to shield its planetary atmosphere from erosion by stellar activity such as coronal mass ejections (Kay et al. 2016). Early-type M dwarfs are also more abundant than Sun-like stars and have larger HZs and less activity than other types of M dwarfs (Heller & Armstrong 2014; Cuntz & Guinan 2016). Hence we could call early-type M dwarfs "Goldilocks M dwarfs" for the search of habitable worlds.

To date, the transit and RV methods have been used to discover about 20 Earth-sized HZ planets around M dwarfs. Most of these temperate worlds are around late-type M dwarfs, such as Proxima b, (Anglada-Escudé et al. 2016), Teegarden's Star b (Zechmeister et al. 2019), and the TRAPPIST-1 system (Gillon et al. 2017). To increase the sample of Earth analogs, the RV community has collected precision RV data for a few decades using spectrometers such as the High Accuracy Radial velocity Planet Searcher (HARPS; Pepe et al. 2002), the Planet Finder Spectrograph (PFS; Crane et al. 2006, 2008, 2010), and the High Resolution Echelle Spectrometer mounted on a Keck telescope (HIRES/Keck; Vogt et al. 1994). In particular, many infrared spectrographs including the Calar Alto high-Resolution search for M dwarfs with Exo-earths with Near-infrared and optical Echelle Spectrographs (CARMENES; Quirrenbach et al. 2010), the Infrared Doppler Instrument (IRD; Tamura et al. 2012), the Habitable Zone Planet Finder (HPF; Mahadevan et al. 2012), and the SPectopolarimètre

[7] Hubble Fellow.
[8] http://www.recons.org/census.posted.htm

Table 1
Stellar Parameters and RV Data Sets

Star	Other Name	Type	Stellar Mass ($M_\star$)	Parallax (mas)	V (mag)	APF	H1	H2	Keck	PFS	SOPHIE
GJ 2056	HIP 34785	M0	0.62 ± 0.08	35.13 ± 0.03	10.3	0	15	0	0	51	0
GJ 317	LHS 2037	M3.5V	0.42 ± 0.02	65.77 ± 0.06	12	0	84	48	66	32	0
GJ 480	HIP 61706	M3.5Ve	0.45 ± 0.02	70.22 ± 0.07	11.5	0	37	0	21	0	0
GJ 687	HIP 86162	M3.0V	0.40 ± 0.02	219.78 ± 0.03	9.2	149	0	0	147	0	0
GJ 9066	GJ 83.1	M4.5V	0.15 ± 0.02	223.63 ± 0.11	12.5	0	25	0	54	0	0
HIP 107772	TYC 7986-911-1	M0V	0.63 ± 0.08	42.27 ± 0.04	10.5	0	22	0	0	49	0
HIP 38594	TYC 6557-844-1	M0	0.61 ± 0.02	56.19 ± 0.03	9.7	0	17	0	0	38	0
HIP 4845	GJ 3072	M0V	0.62 ± 0.04	47.37 ± 0.04	9.9	0	5	0	36	55	0
HIP 48714	GJ 373	M0.5Ve	0.58 ± 0.02	94.94 ± 0.04	8.9	119	0	0	22	0	12
HIP 60559	Ross 695	M2	0.26 ± 0.02	112.74 ± 0.07	11.3	0	24	0	17	0	0
HIP 67164	GJ 3804	M3.5	0.34 ± 0.02	89.23 ± 0.08	11.9	0	18	0	21	0	0

Note. The stellar type is given by the Simbad database (Wenger et al. 2000). The parallax is from Gaia data release 2 (DR2), the V magnitude is derived from the G magnitude from Gaia DR2 according to Jordi et al. (2010), and the stellar mass is from TESS Input Catalog (TIC; Stassun et al. 2019). To be simple, we use "H1" and "H2," respectively, to denote HARPSpre and HARPSpost in this table. The complete set of newly derived radial velocities is published in its entirety in the machine-readable format in Table 2.

InfraRouge (SPIRou; Artigau et al. 2014) are designed to be sensitive to Earth analogs around M dwarfs. The next generation high precision spectrographs such as the Echelle Spectrograph for Rocky Exoplanet and Stable Spectroscopic Observations (ESPRESSO; Pepe et al. 2010), EXtreme PREcision Spectrometer (EXPRES; Jurgenson et al. 2016), and NEID (Schwab et al. 2016) are able to improve the RV prevision to sub-m s^{-1} level, which is marginally sensitive to Earth twins. While these instruments lay the foundation for extreme precision RV, multiple barriers must be overcome to firmly detect signals caused by Earth analogs in noisy RV data.

Detection of Earth analogs is challenged by instrumental instability (e.g., Halverson et al. 2016 and Bechter et al. 2018), stellar activity (e.g., Dumusque et al. 2014 and Fischer et al. 2016), and biased barycentric correction (e.g., Wright & Eastman 2014 and Feng et al. 2019). In order to improve the efficiency and reliability of the RV method, Feng et al. (2017a) developed the Agatha software suite to provide comprehensive activity diagnoses. Moreover, to improve the barycentric correction precision to 1 cm $^{-1}$ level, Feng et al. (2019) created the PEXO software to correctly model both the Earths barycentric motion and the reflex motion of the target star by accounting for relativistic effects. Recently our group developed an automated Agatha pipeline that has already been used to efficiently detect more than 20 planet candidates in Feng et al. (2019, hereafter Paper I) and Feng et al. (2020, hereafter Paper II). In Paper II, we reported two temperate super-Earths orbiting around early-type M stars, indicating a large population of temperate worlds embedded in the archived RV data. In this work, we continue to use our automated pipeline to search for nearby Earth analogs around M dwarfs, especially early-type ones.

The paper is structured as follows. We introduce the RV data sets used in this work in Section 2 and briefly describe our methodology in Section 3. Then we report the planet candidates in Section 4 and study their dynamical stability in Section 5. Finally, we conclude in Section 6.

2. Data

We select M dwarfs with RV data sets from the Automated Planet Finder (APF; Vogt et al. 2014), HARPS, HIRES/Keck, PFS, and the Spectrographe pour l'Observation des Phénomènes des Intérieurs stellaires et des Exoplanètes (SOPHIE; Perruchot et al. 2008). Based on comprehensive analyses, we identify eleven stars that probably host planets. The physical parameters and the number of RVs in each data set for each star are shown in Table 1. We use HARPSpre and HARPSpost to denote the RV sets obtained before and after the fiber change for HARPS in 2015. Since we have not found discontinuity in RVs obtained before and after upgrade of the PFS detector, we do not treat them independently as we did in Paper I and II.

Table 2
Newly Derived RVs

Star	BJD (day)	RVel (m s^{-1})	σ_{RVel} (m s^{-1})	Instr
GJ 2056	2455200.70457	2.44	2.8	PFS
GJ 2056	2455200.70888	1.89	3.18	PFS
GJ 2056	2455255.60378	−9.03	1.7	PFS
GJ 2056	2455581.63635	−4.39	1.39	PFS
GJ 2056	2455669.51865	−2.09	1.46	PFS
GJ 2056	2455953.71928	−0.57	2.77	PFS
GJ 2056	2455955.68571	−7.3	1.18	PFS
GJ 2056	2455957.63083	3.89	2.56	PFS

(This table is available in its entirety in machine-readable form.)

As described in Paper I and II, the Keck data was reduced and released by Butler et al. (2017), and the PFS data are reduced using the method developed by Butler et al. (1996, 2006). We use the HARPS data reduced by Trifonov et al. (2020) using the SERVAL pipeline (Zechmeister et al. 2018). The nightly RV zero-points are subtracted from the reduced data to reduce systematics. In addition to the data sets used in Paper II, we use the SOPHIE data released by Soubiran et al. (2018) with correction of zero-point drift (Courcol et al. 2015). Moreover, we use the RV data obtained by the Levy spectrometer mounted on the 2.4 m APF telescope. The APF data is reduced using the same pipeline as used for PFS data reduction. The newly derived RV data from PFS, KECK, APF, and SOPHIE are partly shown in Table 2 and are available in the machine-readable table.

To compare the instrumental stabilities of APF (237 stars), PFS (573 stars), HARPSpre (2678 stars), HARPSpost (917 stars), and Keck (1700 stars), we select the stars with more than 50 RVs and with standard deviations of less than 5, 10, and 20 m s^{-1} for each instrument. We bin the data using a 10 day time bin and calculate the weighted mean for each instrument.

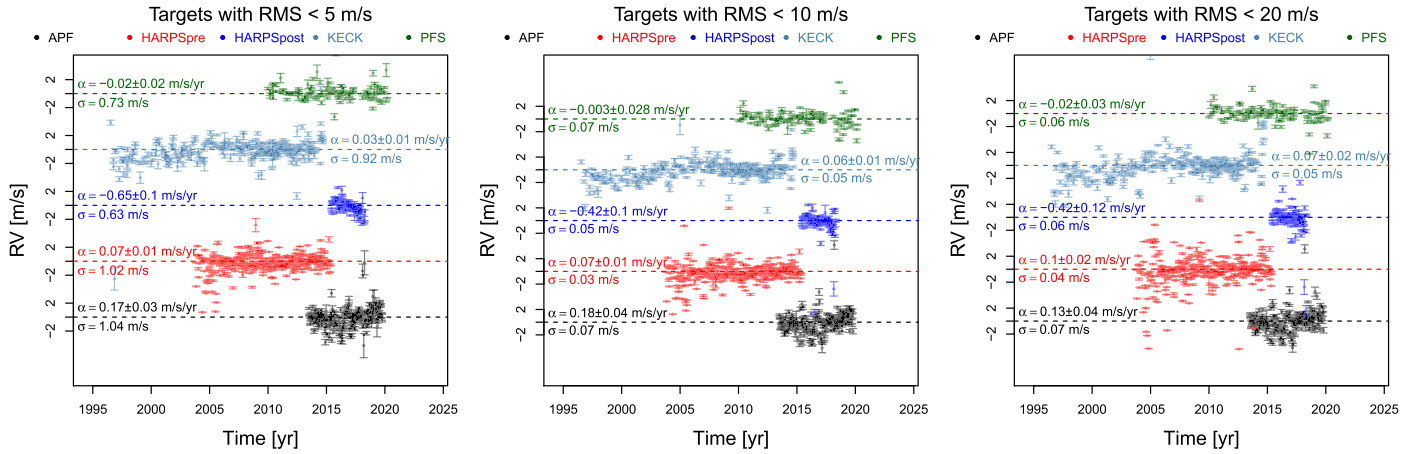

Figure 1. Comparison of the instrumental stability of APF, HARPSpre, HARPSpost, Keck, and PFS. The averaged RVs for different instruments are color-coded and shifted to optimize visualization. The slope (α) and the standard deviation (σ) of residuals of the best-fit linear trend is shown for each instrument.

We compare long-term stability of these instruments through robust linear regressions for the averaged data using the R package MASS (Venables & Ripley 2002). The weighted standard deviation (σ) of the residuals are calculated using the R package radiant.data (https://CRAN.R-project.org/package=radiant.data). The results are shown in Figure 1. Since the residuals for rms $< 5\,\mathrm{m\,s^{-1}}$ show much larger scattering than the ones selected by higher rms, we focus our investigation on the targets selected by rms $< 10\,\mathrm{m\,s^{-1}}$, which is more conservative than rms $< 20\,\mathrm{m\,s^{-1}}$.

The slope for the best-fit linear trend is $0.18 \pm 0.04\,\mathrm{m\,s^{-1}\,yr^{-1}}$ for APF, $0.07 \pm 0.01\,\mathrm{m\,s^{-1}\,yr^{-1}}$ for HARPSpre, $-0.42 \pm 0.10\,\mathrm{m\,s^{-1}\,yr^{-1}}$ for HARPSpost, $0.06 \pm 0.01\,\mathrm{m\,s^{-1}\,yr^{-1}}$ for Keck, and $0.003 \pm 0.07\,\mathrm{m\,s^{-1}\,yr^{-1}}$ for PFS. The HARPSpost and APF data show the most significant linear trends, likely due to their shorter observing baselines and smaller amount of RVs, both of which make them more sensitive to RV variations caused by planets and stellar activity. On the other hand, the HARPSpre and Keck sets have longer time spans and more RVs and thus are more suitable for stability analysis. We find $0.06\,\mathrm{m\,s^{-1}\,yr^{-1}}$ and $0.07\,\mathrm{m\,s^{-1}\,yr^{-1}}$ accelerations for Keck and HARPSpre at 6σ and 7σ confidence levels, respectively. The zero-point corrected Keck data (Tal-Or et al. 2019) also show a similar linear trend with a slope of $0.05 \pm 0.01\,\mathrm{m\,s^{-1}\,yr^{-1}}$. Thus the zero-point correction is probably not able to remove long-term bias in RV data. The linear trends are unlikely to be caused by outliers because they appear in the RV data selected by different criteria. Moreover, the linear fits are weighted by measurement errors, reducing the influence of outliers that typically have large error bars. Hence the similar acceleration shared by Keck and HARPSpre that suggests a common astrophysical origin such as relativistic effects in the solar system as mentioned in Feng et al. (2019). There are also linear trends in APF and HARPS data with a significance of about 4σ. Compared with the other instruments, PFS is the most stable instrument over decade-long timescales. The residuals for all instruments are less than $0.1\,\mathrm{m\,s^{-1}}$ and HARPSpre shows slightly better short-term stability. The instability bias in the data sets we use in this study is much less than $1\,\mathrm{m\,s^{-1}}$ and is thus negligible for the data analysis in this work. The SOPHIE data has larger uncertainty even after drift correction and thus only plays a minor role in the constraints of orbits. Hence their instrumental instability is less important for this work.

3. Method

3.1. RV Model

Following Paper I and II, we model the RV variation at epoch t_j of data set k induced by planets using

$$\hat{v}^k_{p,j} = \sum_{i=1}^{N_p} K_i[\sin(\omega_i + \nu_i(t_j)) + e_i \cos\omega_i] + \gamma_k\,, \qquad (1)$$

where N_p is the number of planetary signals, K_i is the semi-amplitude of the RV variation induced by planet i, γ_k is the offset of RV set k, ω_i is the argument of periastron of planet i, e_i is eccentricity, $\nu_i(t_j)$ is the true anomaly of planet i at epoch t_j and can be derived from the reference mean anomaly $M_j(t_0)$ (or $M_{0,j}$), and period P_j by solving Kepler's equation. Here we do not use a linear trend to model acceleration to avoid potential degeneracy between the linear trend and long-period planet signals.

We use the moving average (MA) model to account for time correlated noise (or red noise) in RV data induced by stellar activity and instrumental instability. Thus the full model for the RV at epoch t_j of set k is

$$\hat{v}^k_j = \hat{v}^k_{p,j} + \sum_{n=1}^{q} w^k_n \exp\left(-\frac{|t_j - t_{j-n}|}{\tau_k}\right)(v^k_{j-n} - \hat{v}^k_{p,j-n})\,, \qquad (2)$$

where q is the order of the MA model, w^k_n is the amplitude of MA component n for set k, τ_k is the correlation timescale for set k, v^k_{j-n} is the observed RV at epoch t_{j-n} of set k, and $\hat{v}_{p,j-n}$ is the Keplerian RV at epoch t_{j-n} of set k. The MA model is found to be the so-called "Goldilocks model," which is able to avoid false positives and false negatives according to the study of synthetic and real RV sets (Feng et al. 2016; Ribas et al. 2018) as well as the RV fitting challenge (Dumusque et al. 2017). Following Feng et al. (2017a), we compare different orders of MA models in the Bayesian framework. Specifically, we select the highest order q, which passes the criterion that the relative Bayesian information criterion (ΔBIC; Spiegelhalter et al. 2002) of MA(q) relative to MA($q-1$) is larger than 10 (Kass & Raftery 1995; Feng et al. 2016).

Table 3
Parameters for the Planet Candidates

Planet	$M_p \sin I$ ($M_\oplus$)	a (au)	P (day)	K (m s^{-1})	e	ω (deg)	T_p (JD-2400000)	lnBF$_3$	Note
GJ 2056 b	16.2 ± 3.6	0.283 ± 0.013	69.971 ± 0.061	5.23 ± 1.51	0.72 ± 0.10	58 ± 116	52965.6 ± 3.5	10.4	HZ
	$17.6^{+7.8}_{-8.6}$	$0.283^{+0.027}_{-0.033}$	$69.937^{+0.199}_{-0.164}$	$4.89^{+3.97}_{-2.29}$	$0.64^{+0.26}_{-0.17}$	13^{+347}_{-12}	$52967.9^{+9.1}_{-11.5}$		
GJ 2056 c	141.2 ± 17.0	3.453 ± 0.164	2982.394 ± 75.913	14.59 ± 1.10	0.81 ± 0.02	338 ± 69	50505.3 ± 156.1	15.0	PC
	$141.2^{+39.9}_{-39.0}$	$3.469^{+0.337}_{-0.436}$	$2996.577^{+178.294}_{-170.268}$	$13.92^{+2.97}_{-1.97}$	$0.79^{+0.06}_{-0.04}$	349^{+11}_{-349}	$50472.0^{+339.4}_{-378.0}$		
GJ 317 b	557.1 ± 18.3	1.151 ± 0.018	695.660 ± 0.355	71.81 ± 0.58	0.07 ± 0.01	72 ± 133	50988.9 ± 14.5	256.2	A12
	$556.1^{+43.3}_{-42.3}$	$1.152^{+0.040}_{-0.045}$	$695.890^{+0.619}_{-1.100}$	$71.59^{+1.81}_{-1.11}$	$0.07^{+0.02}_{-0.02}$	6^{+353}_{-6}	$50986.2^{+33.6}_{-29.2}$		
GJ 317 c	522.5 ± 19.1	5.230 ± 0.111	6739.323 ± 143.106	31.97 ± 0.56	0.17 ± 0.02	108 ± 9	49804.6 ± 221.5	58.7	A12
	$529.0^{+37.6}_{-52.9}$	$5.223^{+0.268}_{-0.251}$	$6718.777^{+375.180}_{-282.469}$	$32.36^{+0.84}_{-1.77}$	$0.17^{+0.05}_{-0.05}$	114^{+18}_{-26}	$49916.0^{+436.8}_{-611.2}$		
GJ 480 b	13.2 ± 1.7	0.068 ± 0.001	9.567 ± 0.005	6.80 ± 0.87	0.10 ± 0.07	151 ± 92	54562.1 ± 2.3	19.7	
	$13.5^{+3.8}_{-4.4}$	$0.068^{+0.002}_{-0.003}$	$9.565^{+0.015}_{-0.009}$	$6.92^{+1.96}_{-2.20}$	$0.04^{+0.25}_{-0.03}$	118^{+235}_{-114}	$54562.5^{+4.0}_{-5.2}$		
GJ 687 b	17.2 ± 1.0	0.163 ± 0.003	38.142 ± 0.007	6.14 ± 0.32	0.17 ± 0.05	117 ± 19	50592.7 ± 2.0	95.4	HZ, B14
	$17.2^{+2.4}_{-2.5}$	$0.163^{+0.006}_{-0.007}$	$38.145^{+0.015}_{-0.020}$	$6.15^{+0.67}_{-0.79}$	$0.19^{+0.10}_{-0.14}$	127^{+34}_{-62}	$50593.6^{+3.3}_{-6.6}$		
GJ 687 c	16.0 ± 4.1	1.165 ± 0.023	727.562 ± 12.198	2.44 ± 0.80	0.40 ± 0.22	176 ± 63	50304.1 ± 292.8	10.7	
	$19.4^{+5.2}_{-12.4}$	$1.164^{+0.056}_{-0.054}$	$726.403^{+39.189}_{-29.204}$	$3.69^{+0.56}_{-2.74}$	$0.72^{+0.03}_{-0.71}$	189^{+160}_{-178}	$49891.9^{+710.3}_{-16.1}$		
GJ 9066 b	30.9 ± 6.4	0.403 ± 0.018	241.883 ± 1.808	11.53 ± 2.28	0.18 ± 0.12	204 ± 129	51273.4 ± 50.7	12.0	
	$27.9^{+19.0}_{-11.0}$	$0.403^{+0.039}_{-0.047}$	$241.590^{+4.635}_{-3.996}$	$10.29^{+6.53}_{-3.73}$	$0.16^{+0.32}_{-0.16}$	5^{+353}_{-3}	$51287.1^{+119.4}_{-111.3}$		
GJ 9066 c	71.6 ± 10.3	0.870 ± 0.040	767.887 ± 7.500	18.97 ± 2.13	0.33 ± 0.10	278 ± 119	50884.0 ± 53.3	20.4	
	$70.7^{+26.3}_{-21.5}$	$0.871^{+0.086}_{-0.100}$	$766.954^{+16.710}_{-19.237}$	$18.98^{+5.69}_{-4.81}$	$0.39^{+0.18}_{-0.32}$	331^{+29}_{-330}	$50870.5^{+148.8}_{-121.9}$		
HIP 107772 b	12.9 ± 3.0	0.243 ± 0.011	55.199 ± 0.083	3.01 ± 0.65	0.18 ± 0.11	151 ± 72	53199.6 ± 11.2	8.7	HZ
	$15.6^{+4.6}_{-9.4}$	$0.243^{+0.022}_{-0.027}$	$55.259^{+0.111}_{-0.311}$	$3.63^{+0.96}_{-2.13}$	$0.21^{+0.25}_{-0.20}$	163^{+184}_{-152}	$53199.0^{+28.9}_{-22.4}$		
HIP 38594 b	8.1 ± 1.7	0.256 ± 0.003	60.722 ± 0.122	1.89 ± 0.40	0.17 ± 0.11	125 ± 100	52956.2 ± 13.9	6.2	HZ
	$8.2^{+3.8}_{-4.3}$	$0.256^{+0.006}_{-0.007}$	$60.711^{+0.426}_{-0.192}$	$1.90^{+0.91}_{-1.00}$	$0.19^{+0.28}_{-0.18}$	42^{+315}_{-39}	$52948.1^{+40.8}_{-17.7}$		
HIP 38594 c	48.4 ± 7.4	3.805 ± 0.172	3477.768 ± 229.001	2.89 ± 0.42	0.16 ± 0.10	196 ± 68	51246.7 ± 1337.9	11.2	
	$42.9^{+24.5}_{-11.2}$	$3.842^{+0.399}_{-0.441}$	$3524.860^{+540.850}_{-572.002}$	$2.60^{+1.31}_{-0.66}$	$0.26^{+0.16}_{-0.25}$	231^{+114}_{-207}	$49725.1^{+3247.8}_{-457.2}$		
HIP 4845 b	14.4 ± 3.0	0.176 ± 0.007	34.150 ± 0.046	4.05 ± 0.86	0.25 ± 0.14	108 ± 72	54702.0 ± 5.6	13.0	
	$16.7^{+5.2}_{-9.0}$	$0.177^{+0.016}_{-0.020}$	$34.151^{+0.170}_{-0.090}$	$4.79^{+1.40}_{-2.61}$	$0.36^{+0.21}_{-0.35}$	87^{+262}_{-79}	$54701.3^{+19.2}_{-12.4}$		
HIP 48714 b	22.9 ± 2.8	0.112 ± 0.001	17.818 ± 0.002	9.35 ± 1.29	0.50 ± 0.08	202 ± 14	51539.8 ± 1.0	23.4	
	$22.5^{+7.2}_{-6.3}$	$0.112^{+0.003}_{-0.003}$	$17.819^{+0.004}_{-0.009}$	$9.56^{+2.99}_{-3.17}$	$0.57^{+0.11}_{-0.27}$	202^{+37}_{-31}	$51539.6^{+4.1}_{-1.9}$		
HIP 60559 b	15.9 ± 3.8	0.297 ± 0.008	115.796 ± 0.493	5.27 ± 1.26	0.21 ± 0.11	257 ± 99	51474.3 ± 32.8	11.6	NC
	$17.1^{+9.8}_{-8.9}$	$0.298^{+0.017}_{-0.019}$	$115.873^{+0.837}_{-1.585}$	$5.70^{+2.96}_{-3.05}$	$0.28^{+0.21}_{-0.27}$	299^{+59}_{-297}	$51454.6^{+96.8}_{-17.9}$		
HIP 67164 b	9.7 ± 2.3	0.067 ± 0.001	10.942 ± 0.004	6.06 ± 1.62	0.21 ± 0.16	175 ± 76	51576.6 ± 2.4	12.3	NC
	$11.8^{+3.6}_{-7.5}$	$0.067^{+0.003}_{-0.003}$	$10.941^{+0.008}_{-0.007}$	$9.30^{+1.35}_{-6.67}$	$0.66^{+0.02}_{-0.66}$	177^{+176}_{-170}	$51576.8^{+5.0}_{-5.5}$		

Note. For each parameter, the value at the maximum a posteriori (MAP) and the uncertainty interval defined by the 1% and 99% quantiles of the posterior distribution are shown below the values of mean and standard deviation. $M_p \sin I$ is the minimum planet mass and a is the semimajor axis. These two quantities are derived from the orbital period P, semi-amplitude K, and eccentricity e by using the stellar masses given in Table 1. ω is the argument of periastron, and T_p is the epoch at the periastron. As introduced in Section 3, ln BF$_3$ is the logarithmic Bayes factor of the model including the candidate relative to the model excluding the candidate. Following Paper II, we use bold font to denote strong candidates, italic font to denote weak candidates, and normal font to denote confirmation of previous candidates. In the column of "Note," we fill "HZ" for candidates in the HZ, "PHZ" for candidates with orbits partially in the HZ, "A12" for candidates detected by Anglada-Escudé et al. (2012), "B14" for candidates detected by Burt et al. (2014), "NC" for candidates with inconsistent significance over time due to poor sampling, and "PC" for candidates with incomplete phase coverage.

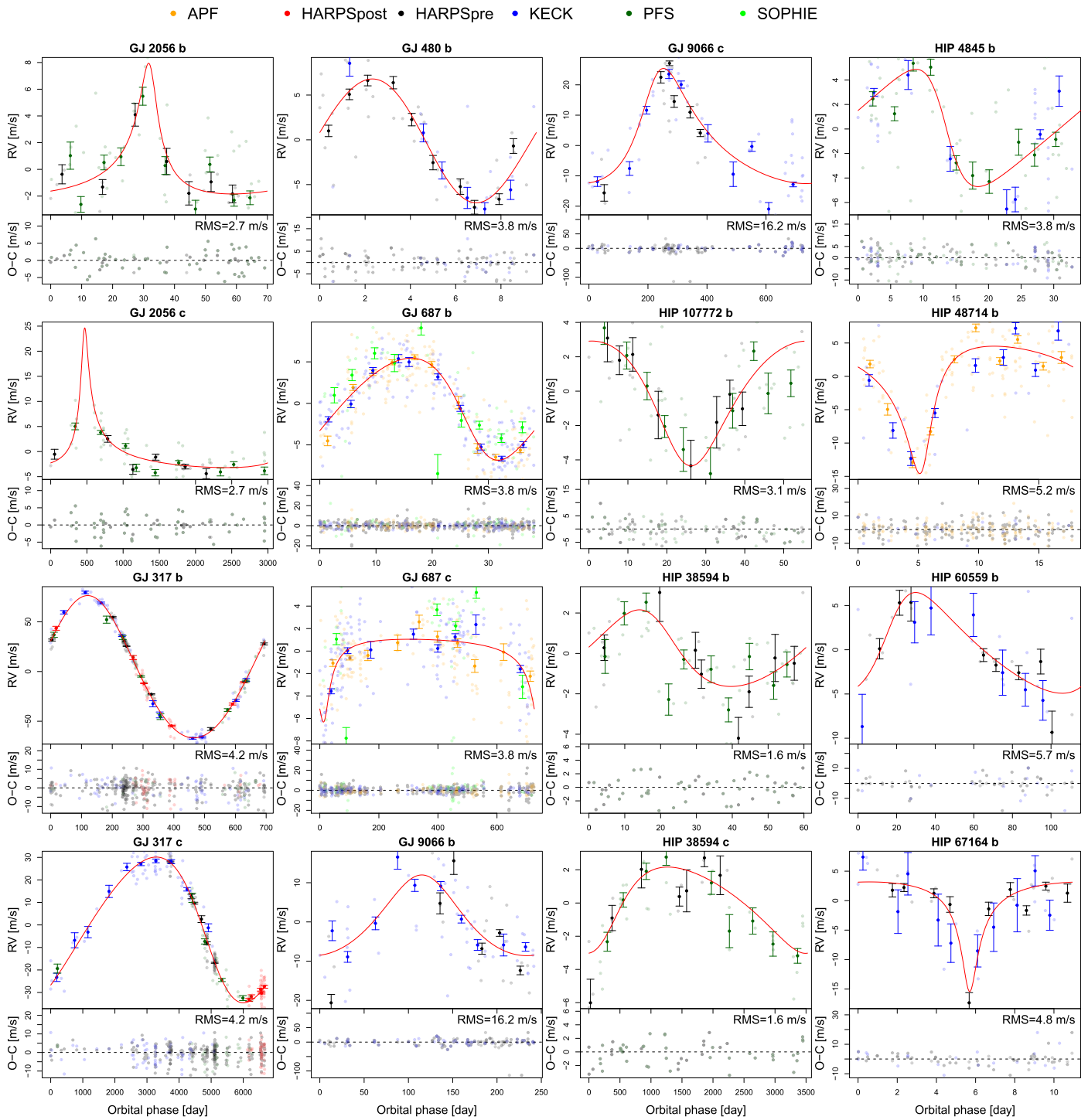

Figure 2. Phase curves and corresponding residuals for all planet candidates are shown. The instruments are encoded by different colors and are shown on top of all panels. The raw data measured by an instrument are binned using 10 time bins that are regularly spaced over the orbital phase. The average and error of the RV for each bin are respectively calculated through weighted averages of the RVs and RV errors in each bin. The best orbital solution is determined by the MAP values of orbital parameters. The rms of the residual RVs after subtracting all signals is shown in each panel.

We model the excess noise in RV data using jitters in the logarithmic likelihood:

$$\ln \mathcal{L} = -\frac{1}{2}\sum_{k=1}^{N_{\rm set}}\sum_{j=1}^{N_k}\left\{\ln\left[2\pi(\sigma_j^k + J_k^2)\right] + \frac{(v_j^k - \hat{v}_j^k)^2}{\sigma_j^k + J_k^2}\right\}, \quad (3)$$

where J_k is the jitter for set k, $N_{\rm set}$ is the total number of RV sets, and N_k is the number of epochs of set k. We adopt logarithmic uniform priors for timescale parameters (P and τ) and a semi-Gaussian prior, $P(e) = \mathcal{N}(\mu = 0,\ \sigma = 0.2)$, for eccentricity to capture the broad feature of nonuniform eccentricity distributions found in Kane et al. (2012) and Van Eylen et al. (2019). The orbital solution is typically robust to the change of σ in the semi-Gaussian prior according to the tests in Paper II. We adopt uniform priors for other parameters. The boundary of these priors are broad enough to allow for all types of orbital solutions.

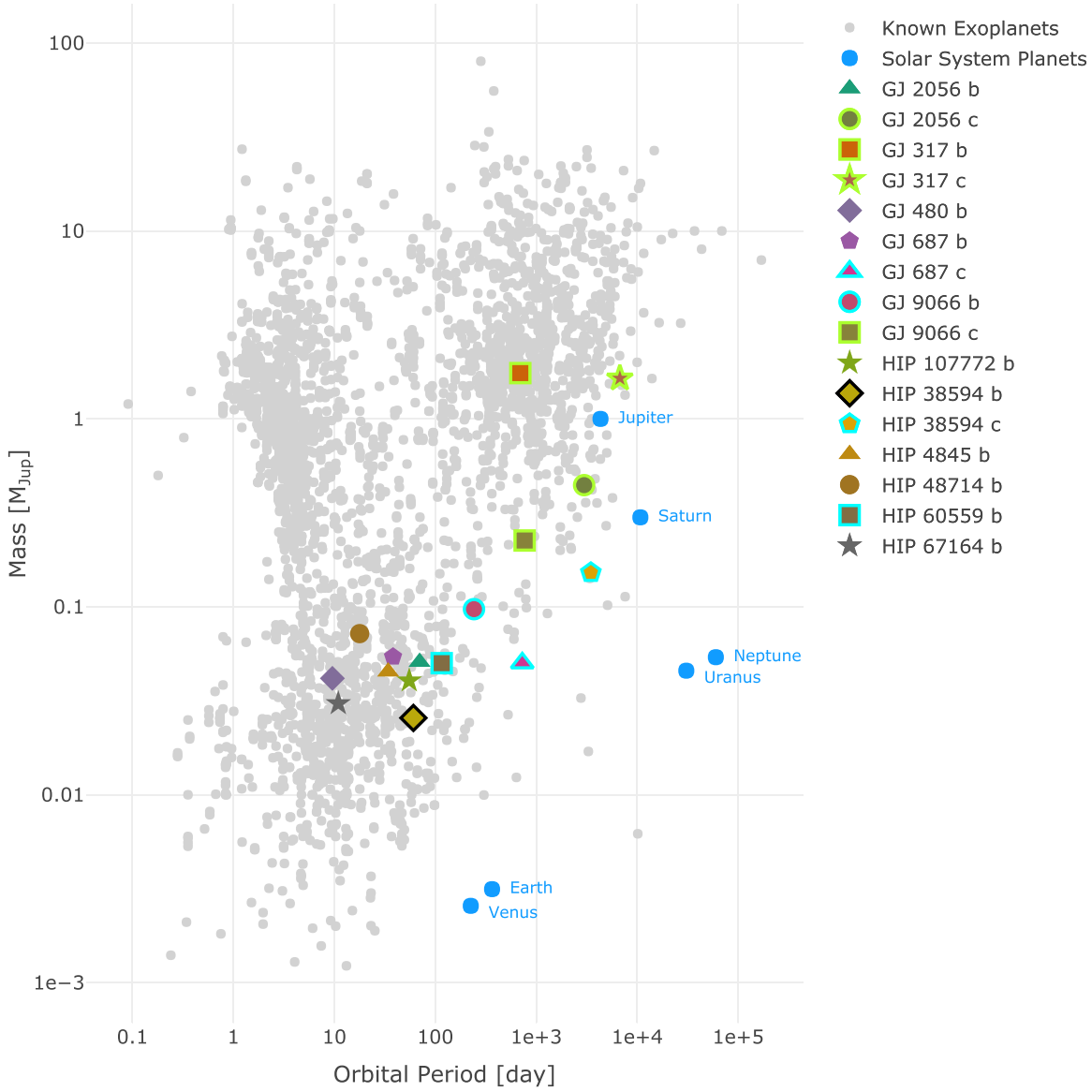

Figure 3. Mass and period distribution of known planets and the planet candidates found in this work. The candidates are represented by different shapes and colors of markers. HIP 38594 b is a temperate super-Earth, denoted by the black-edged diamond marker. The Jupiter analogs are denoted by the yellow–green-edged markers while the cyan-edged markers denote the warm and cold Neptunes detected in this work. The solar system planets are represented by the blue dots.

To explore the posterior, we combine the adaptive Markov Chain Monte Carlo (MCMC) developed by Haario et al. (2001) with a parallel scheme developed in Paper I. Specifically, we launch multiple tempered (hot) chains (typically 16 chains) to explore the global posterior maxima. Then untempered (cold) chains are launched to further sample the global posterior maxima in order to find the optimal solution a posteriori. We start from 0-planet model and repeat these steps for each additional planet until the decrease of BIC is less than 10. Considering that the posterior distributions for multiple-planet systems are typically dominated by a single Gaussian-like distribution, we follow Kass & Raftery (1995) and Feng et al. (2016) to approximate the logarithmic Bayes factor (BF) from ΔBIC using

$$\ln \mathrm{BF} \approx -\frac{1}{2}\Delta\mathrm{BIC} = \mathcal{L}_i^{\max} - \mathcal{L}_{i-1}^{\max} - \frac{1}{2}N_{\mathrm{par}} \ln N_{\mathrm{RV}} , \quad (4)$$

where N_{par} is the effective number of additional free parameters by adding a Keplerian component onto $i-1$ Keplerian components, and N_{RV} is the total number of observed RVs. Thus the $\Delta\mathrm{BIC} > 10$ criterion is equivalent to $\ln \mathrm{BF} > 5$. Since many planetary orbits are approximately circular, eccentricity (e) and the argument of periastron (ω) may not be counted as effective as the other orbital parameters in terms of improving the fitting. Thus we use $\ln \mathrm{BF}_3$ and $\ln \mathrm{BF}_5$, respectively, to denote the ln BFs for a circular solution and an eccentric solution. We stop the MCMC samplers if $\ln \mathrm{BF}_3 < 5$.

3.2. Signal Diagnostics

Following Paper I and II, we diagnose whether an RV signal is related to stellar activity or to planets using four criteria. First, a Keplerian signal should be statistically significant. We regard signals passing $\ln \mathrm{BF}_3 > 5$ as strong and $\ln \mathrm{BF}_5 > 5$ as significant. In other words, the former ones are strong candidates while the latter ones are weak candidates if they satisfy the other criteria as well.

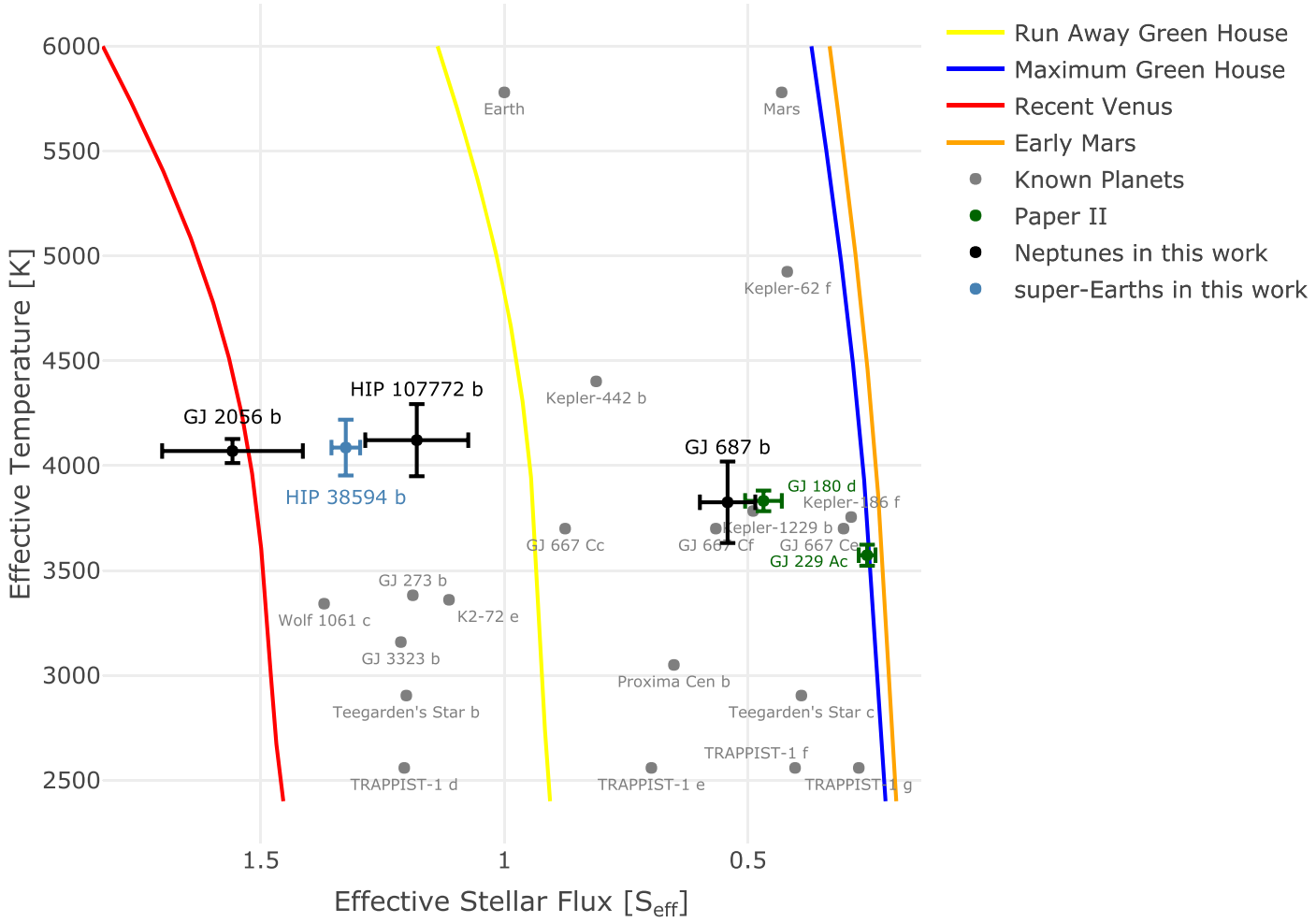

Figure 4. Known planets in the HZ. Based on Monte Carlo samplings of the effective stellar temperature and the stellar flux received by planets, we determine the error bars for the temperate planets detected in Paper II (dark green), the HZ Neptunes (black), and the HZ super-Earth (light blue) found in this work.

Second, a Keplerian signal should be robust to the choice of noise models. To implement this criterion, we calculate the Bayes factor periodograms (BFPs; Feng et al. 2017a) for signals identified in a combined RV set. We compare BFPs calculated using the MA(1) model (or "MA" for abbreviation), the first order autoregressive (AR(1) or "AR" as an abbreviation; Tuomi & Anglada-Escudé 2013) model and the white noise (denoted by "white") model for each signal. The previous signals are subtracted from the raw data for the calculation of BFPs for subsequent signals. Unlike traditional periodograms, a BFP models excess white noise using jitter and models correlated noise using red noise models such as MA and AR. The default red noise model is MA, which is found to be appropriate for RV data (Feng et al. 2016). For a given signal and a noise model, we calculate the BF for each of a sample of periods by maximizing the likelihood using the Marquardt–Levenberg algorithm (Levenberg 1944; Marquardt 1963). The $\ln \mathrm{BF} > 5$ criterion is then used as a threshold to assess the statistical significance of a signal. However, the BFP is not suitable for highly eccentric signals due to the assumption of circular orbits. Hence we only use BFPs to test the sensitivity of signal-to-noise models but rely on MCMCs to fully explore the posterior.

Third, a Keplerian signal should not overlap with the periodic signals found in activity indices or noise proxies. To search for activity signals in noise proxies, we calculate BFPs for the sodium D lines, Hα, the Ca II H and K lines, and their corresponding S-index measurements, along with the bisector and full width of half maximum (FWHM) of spectral lines. We also count the window function as a noise proxy, which is used to exclude aliases and sampling biases. If an RV signal is found to overlap with significant activity signals, it is unlikely to be Keplerian. However, the chance of a random Keplerian signal overlapping with signals in noise proxies is proportional to the number of proxies. In addition, long period signals are more likely to overlap with activity signals because their posterior are less constrained due to sparser sampling of the orbit compared with short period signals. We typically adopt $|P_{\mathrm{rv}} - P_{\mathrm{act}}| < 0.1P_{\mathrm{rv}}$ as a criterion to confirm significant overlap.

Fourth, a Keplerian signal should be consistent over time. We calculate the so-called moving periodogram (MP; Feng et al. 2017a) to implement this criterion. To calculate MP, we define a time window and calculate the BFP for the data covered by this time window. The MA(1) noise model is used by default to account for red noise. We move the time window with a certain time step and calculate the BFP for each step until the whole time span is covered. The sequence of BFPs form a two-dimensional periodogram, called MP. If the signal is consistently significant over time in MP, we regard it as time invariant and probably Keplerian. The time step is adjusted according to the sampling and regularity of the combined data.

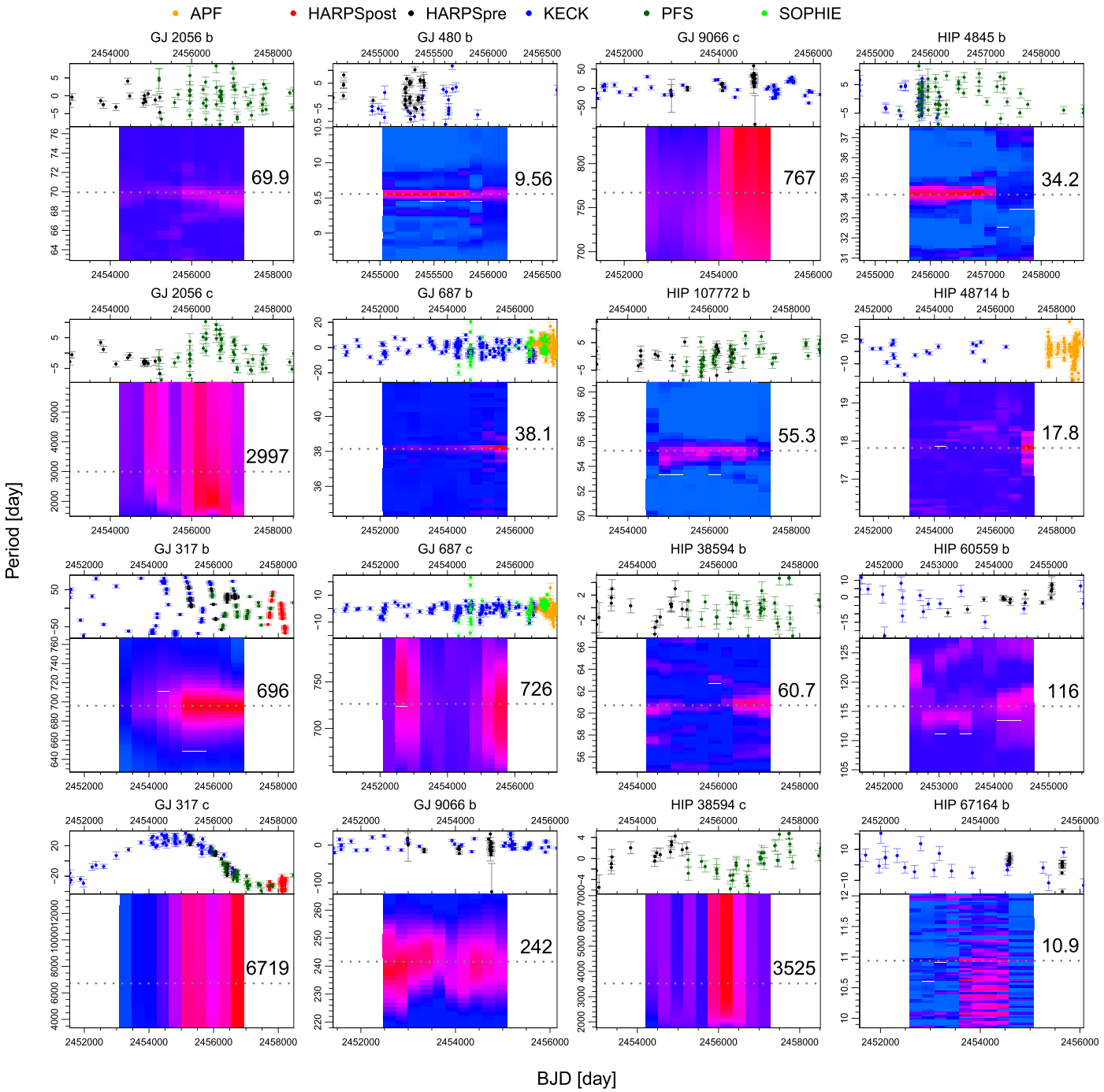

Figure 5. MPs for 16 signals. The width of the time window ΔT is half of the time span (T) of the combined RV data set, i.e., $\delta T = T/2$. The time step is $\delta T = T/20$. It takes 20 steps for the moving time window to cover the whole time span. For each plot, the upper panel shows the data minus the noise component and other RV signals. The optimal parameters of these model components are the MAP values. The lower panel is a zoomed-in view of the whole MP. The signal periods are denoted by horizontal dashed lines and the MAP values in unit of days.

For example, if there is a great gap between two chunks of data, we may choose two time windows and adjust time steps such that each window cover each chunk of the data. An optimal time window should be several orbital periods of a signal but also be small enough to select at most half of the combined data. However, long period signals may not be appropriate for MP because no time window is wide enough to cover one or two periods. A rule of thumb is to calculate MP for signals with periods much shorter than the data baseline (T), to set the window size to be $T/2$, and to define a time step such that the time window covers the whole baseline in 10 steps. To calculate the MPs consistently for different data sets, we use a time window with a size of $T/2$ and a time step of $T/20$ by default.

Finally, we combine the above four critera with eye inspection of the MP, the goodness of fit, and phase coverage of signals to diagnose and classify RV signals.

4. Planet Candidates

There is flexibility in the four criteria introduced in Section 3.2 for signal selection. For example, the criterion of ln(BF) > 5 depends on which number of efficient parameters one chooses to

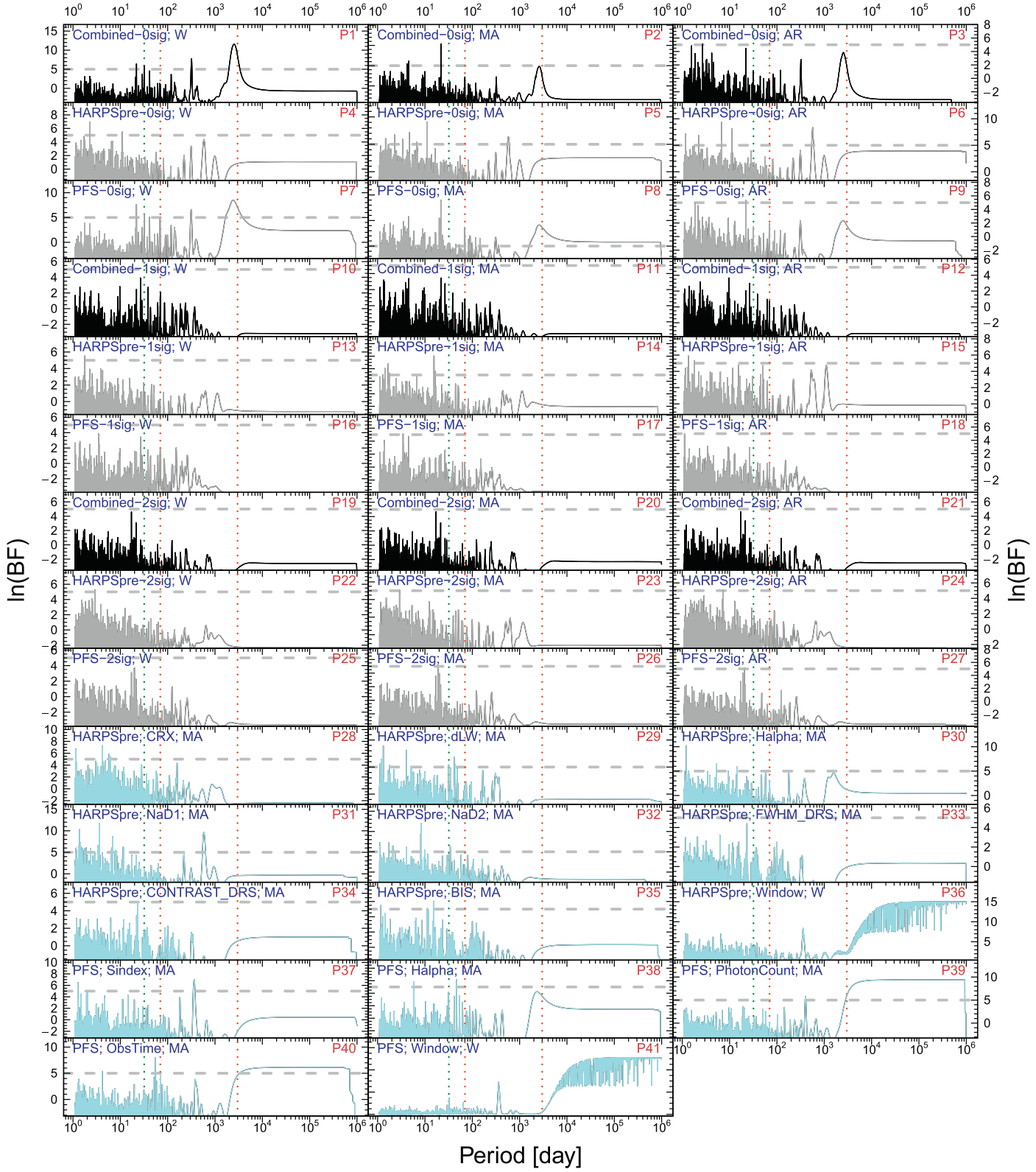

Figure 6. BFPs for the RVs and noise proxies for GJ 2056. The black BFPs are for the combined RV set with signals subtracted subsequently. The gray BFPs are for individual data sets, and the cyan BFPs are for noise proxies. The ln(BF) = 5 threshold is denoted by the dashed lines. The window function is calculated using the Lomb–Scargle periodogram (Lomb 1976; Scargle 1982). To be efficient, we use the generalized Lomb–Scargle periodogram with a floating trend (GLST; Feng et al. 2017a) to show the signals in photometric data. The dark green dotted lines denote the rotation period of 32 days from the literature. The red lines denote the two Keplerian signals at periods of 69.9 and 2997 days. The data and noise model for a BFP is given in the top left corner. The white noise, MA, and AR models are dubbed by "W," "MA," and "AR," respectively. The panel number in each panel is shown for the reader to easily navigate the BFPs. The elements in subsequent BFP figures are defined in the same way.

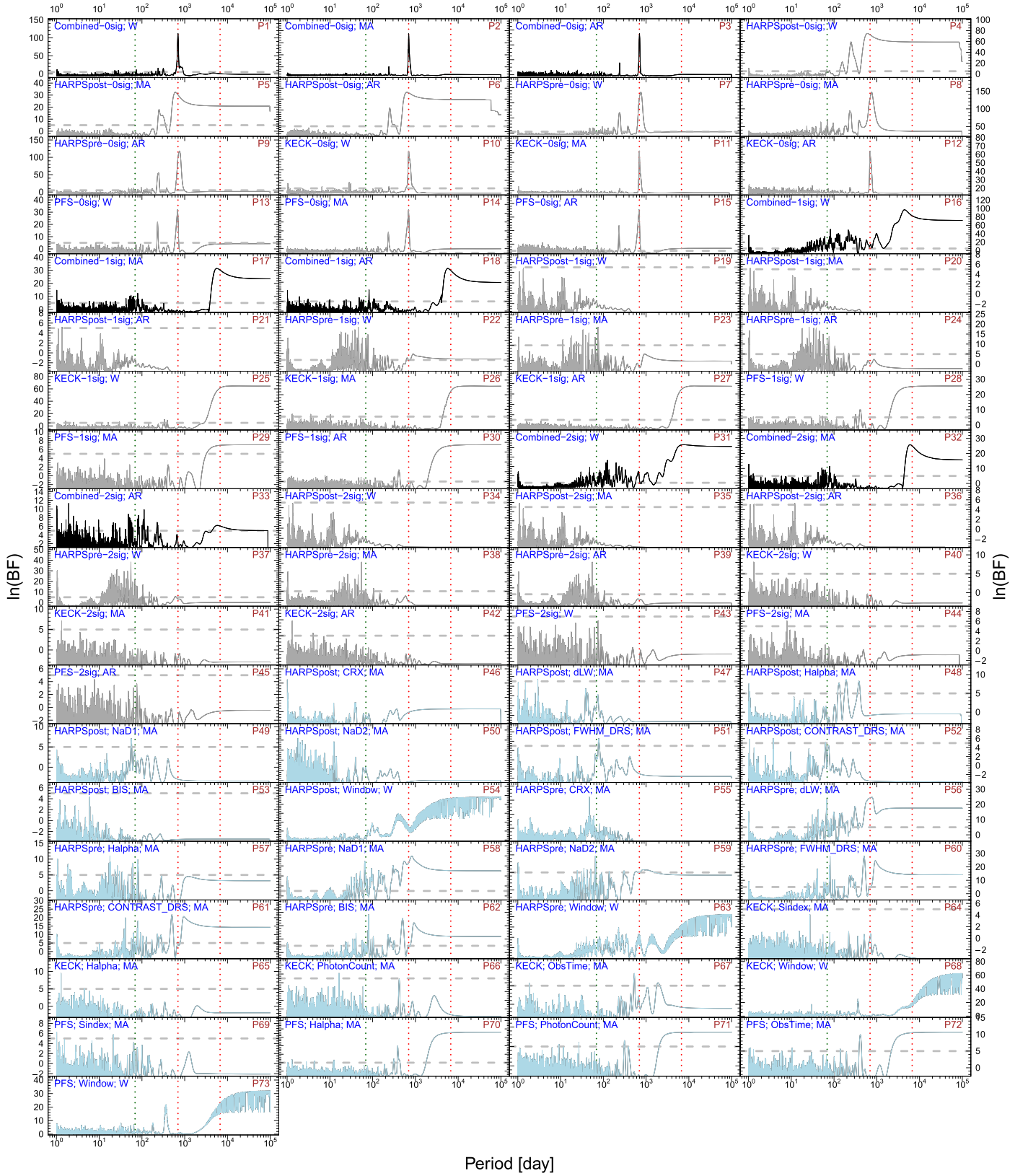

Figure 7. BFPs for the RVs and noise proxies for GJ 317. The dark green dotted lines denote the literature's 69 day rotation period. The red lines denote the 696 and 6719 day Keplerian signals.

calculate ln(BF). The MP criterion depends on the regularity of the data samplings and the quality of the data. Thus we first select primordial signals which pass the $\ln(BF_3) > 5$ criterion. We then investigate the origins of these signals by checking the other criteria. In Section 4.1, we classify the planet candidates into different categories according to the four criteria and study the statistics of these new planet candidates. In Section 4.2, we discuss the results for each target in detail.

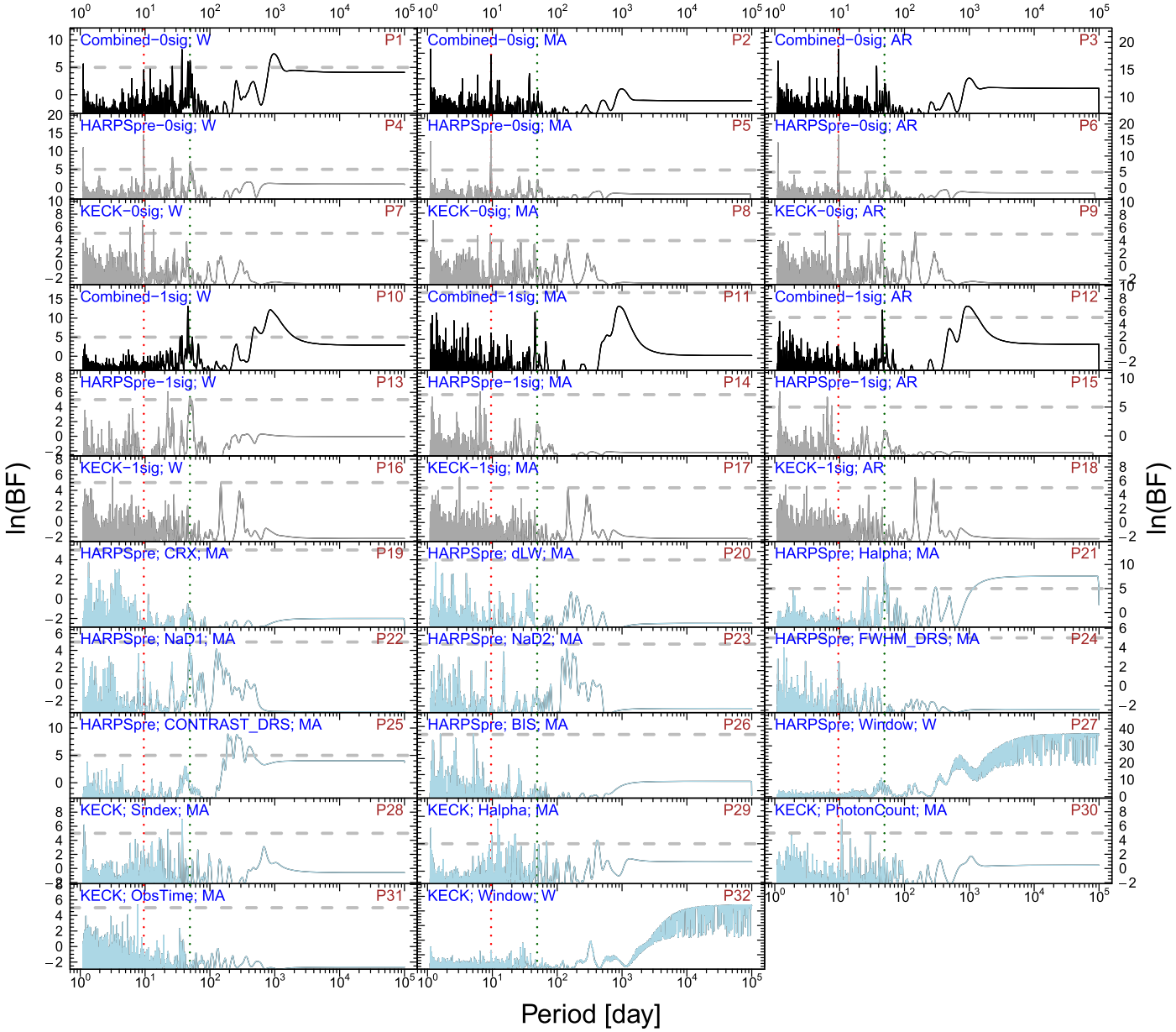

Figure 8. BFPs for the RVs and noise proxies for GJ 480. The dark green dotted lines denote the 49.3 day rotation period determined in this work. The red lines denote the 9.56 day Keplerian signal.

4.1. Statistics of the New Planet Candidates

The parameters of the planet candidates discovered in this work are shown in Table 3. As in Paper II, we classify the candidates into different categories based on the detection criteria we have introduced. There are 10 strong candidates, three weak candidates, and confirmation of three previous candidates. A strong candidate should typically satisfy all of the four criteria. For candidates with periods comparable with the data baseline, we do not apply the time-consistency criterion because the MP is mainly designed to test consistency of short period signals. A weak candidate does not satisfy some criteria due to legitimate reasons such as change in significance caused by highly irregular RV sampling. We will discuss individual cases in Section 4.2.

We show the phase curves for these planet candidates in Figure 2. We also compare our candidates' mass and orbital period distributions to those of other confirmed exoplanets in Figure 3. Thanks to the combined efforts of the RV community, we are able to detect cold Neptunes with periods longer than 100 days and minimum masses between 10 and 60 $M_{\oplus}$, including GJ 687 c, GJ 9066 b, HIP 38594 c, and HIP 60559 b. Our detection of these cold Neptunes contributes significantly to our understanding of this rarely explored population in terms of increasing the sample size for studies of cold Neptune formation. There are seven warm and cold Neptunes detected and two of them also have cold Jupiter companions (GJ 2056 b and c, and GJ 9066 b and c). This is consistent with a positive correlation between super-Earths and cold Jupiters as found by Zhu & Wu (2018) and Bryan et al. (2019), considering that super-Earths and Neptunes are similar in size and mass. The semi-amplitudes of these signals are as low as 1 m s^{-1}, reaching the limit of the current RV precision. Without further improvement of instrument precision and stellar activity modeling, it seems to be quite difficult to probe the $K < 1$ m s^{-1}

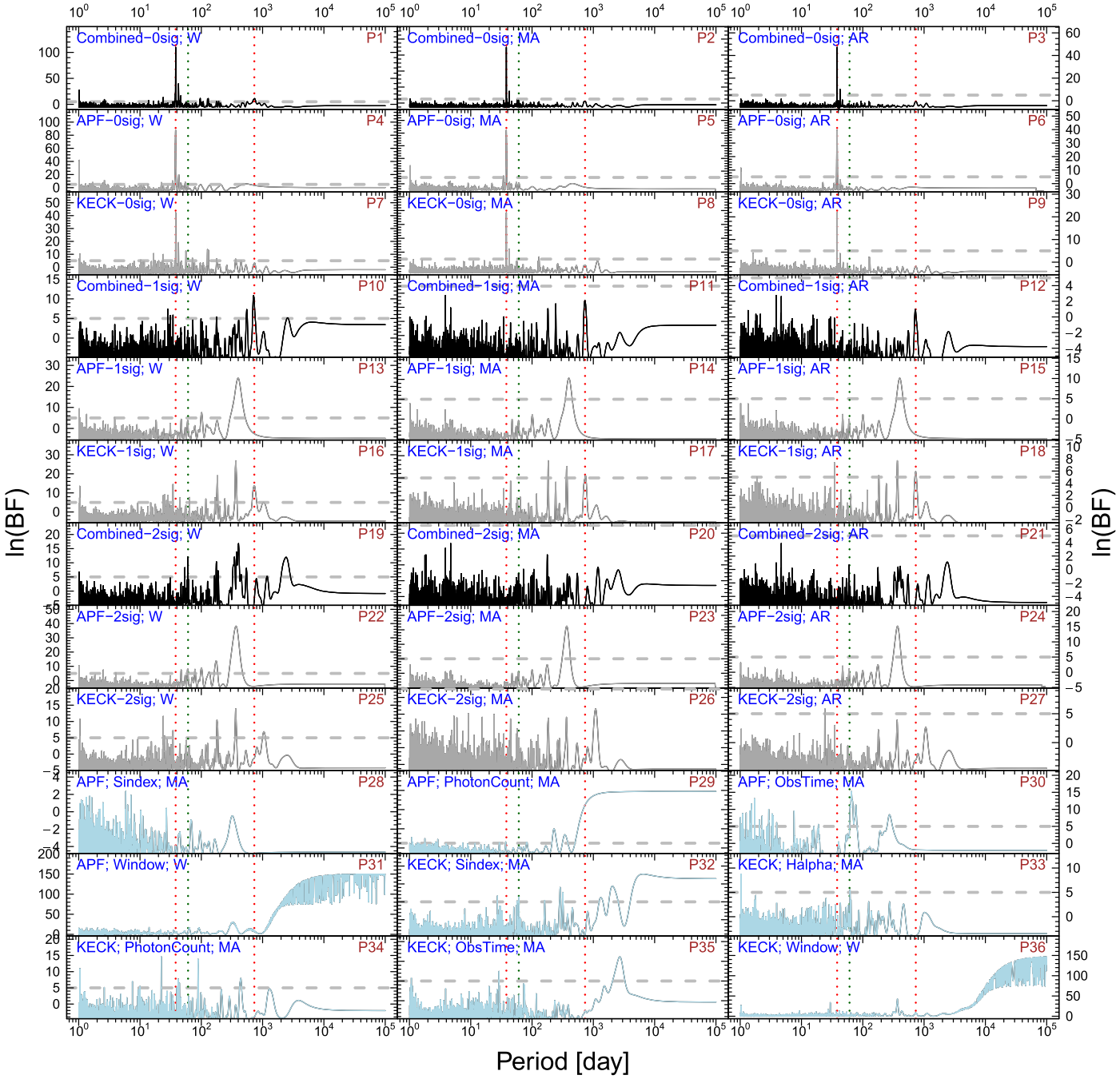

Figure 9. BFPs for the RVs and noise proxies for GJ 687. The dark green dotted lines denote the literature's 60.8 day rotation period. The red lines denote the 38.1 and 726 day Keplerian signals.

regime although sub-m s^{-1} signals have been reported for very stable and intensively observed stars such as τ Ceti (e.g., Feng et al. 2017b). With longer observational baselines and larger compilations of high precision RV measurements, we believe that RV legacy data will play an important role to detect Jupiter analogs that will be observed by the Coronagraph Instrument (CGI) on the Wide Field Infrared Survey Telescope (WFIRST, also named the Roman Space Telescope (RST); Tang et al. 2019), the Mid-Infrared Instrument (MIRI) on the James Webb Space Telescope (Danielski et al. 2018), the wide-field imager Multi-Adaptive Optics Imaging CameraA for Deep Observations (MICADO) mounted on the Extremely Large Telescope (ELT; Perrot et al. 2018) and the Habitable Exoplanet Observatory (HabEx; Gaudi et al. 2020). Such data will also be essential to confirm and characterize the Jupiter analogs found by Gaia (Perryman et al. 2014).

Among the sample of candidates detected in this work, there is a super-Earth candidate (HIP 38594 b) located in the optimistic HZ and three temperate Neptunes (GJ 2056 b, HIP 107772 b, and GJ 687 b) located in the HZ. These planets are shown in the context of the temperate super-Earths reported in Paper II and other previously known HZ planets in Figure 4. Although the potential moons around these temperate Neptunes might host liquid water on their surfaces, they are difficult to detect given the current technology. Hence we focus our investigation on HIP 38594 b, a temperate super-Earth.

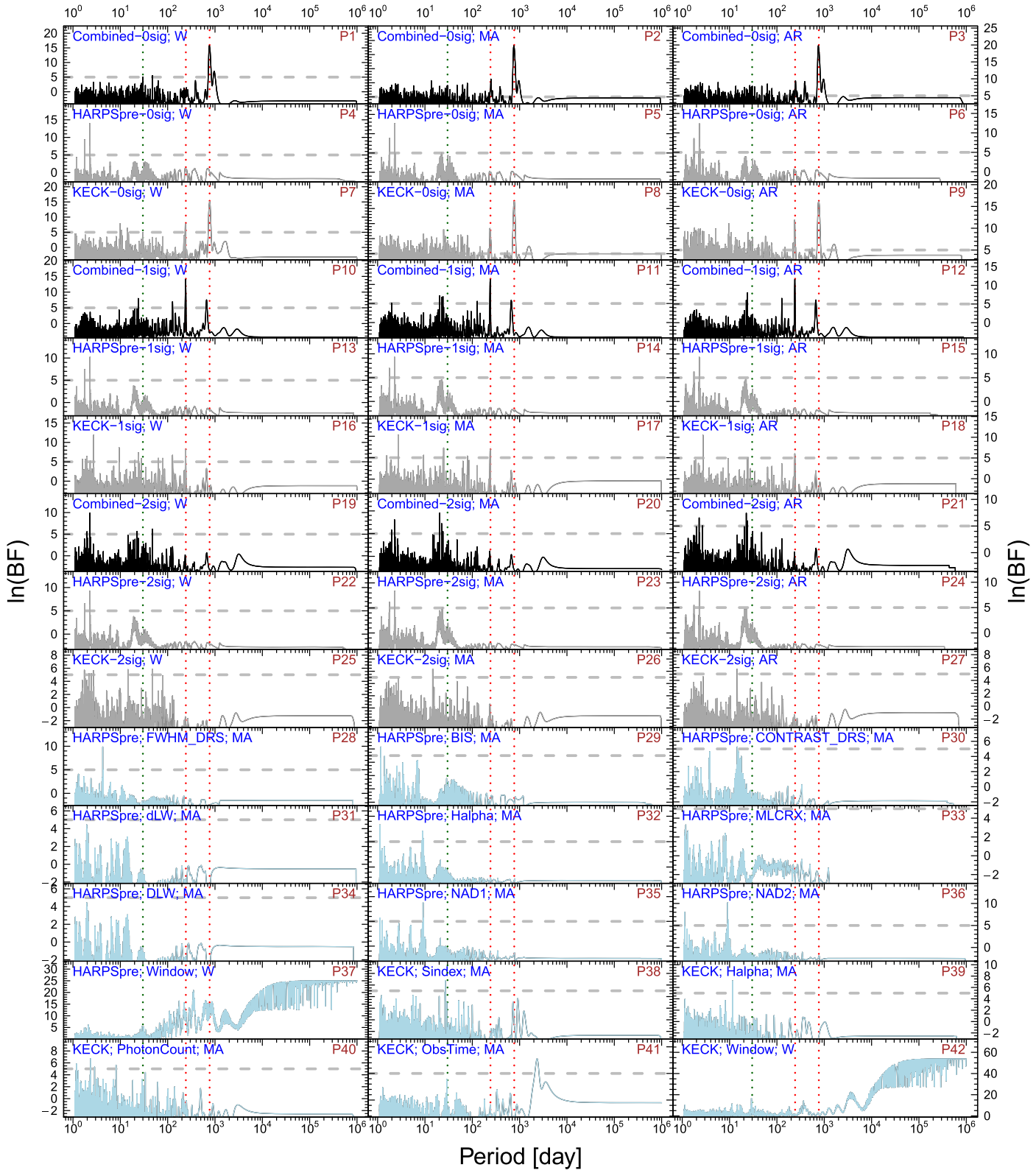

Figure 10. BFPs for the RVs and noise proxies for GJ 9066. The dark green dotted lines denote the literature's 30 day rotation period. The red lines denote the 242 and 773 day Keplerian signals.

Compared with previous M-dwarf hosts of temperate planets, HIP 38594 is an early-type M dwarf and thus is less active in terms of emitting energetic particles and ultraviolet (UV) light (Mohanty & Basri 2003; West et al. 2015). Like K dwarfs, early-type M dwarfs are Goldilocks stellar hosts because they are more abundant than Sun-like stars and have a larger HZ than late-type M dwarfs (Heller & Armstrong 2014; Cuntz & Guinan 2016). HIP 38594 b is separated from HIP 38594 by about 14 mas and would thus make a promising target for direct imaging by ELT/MICADO (Perrot et al. 2018).

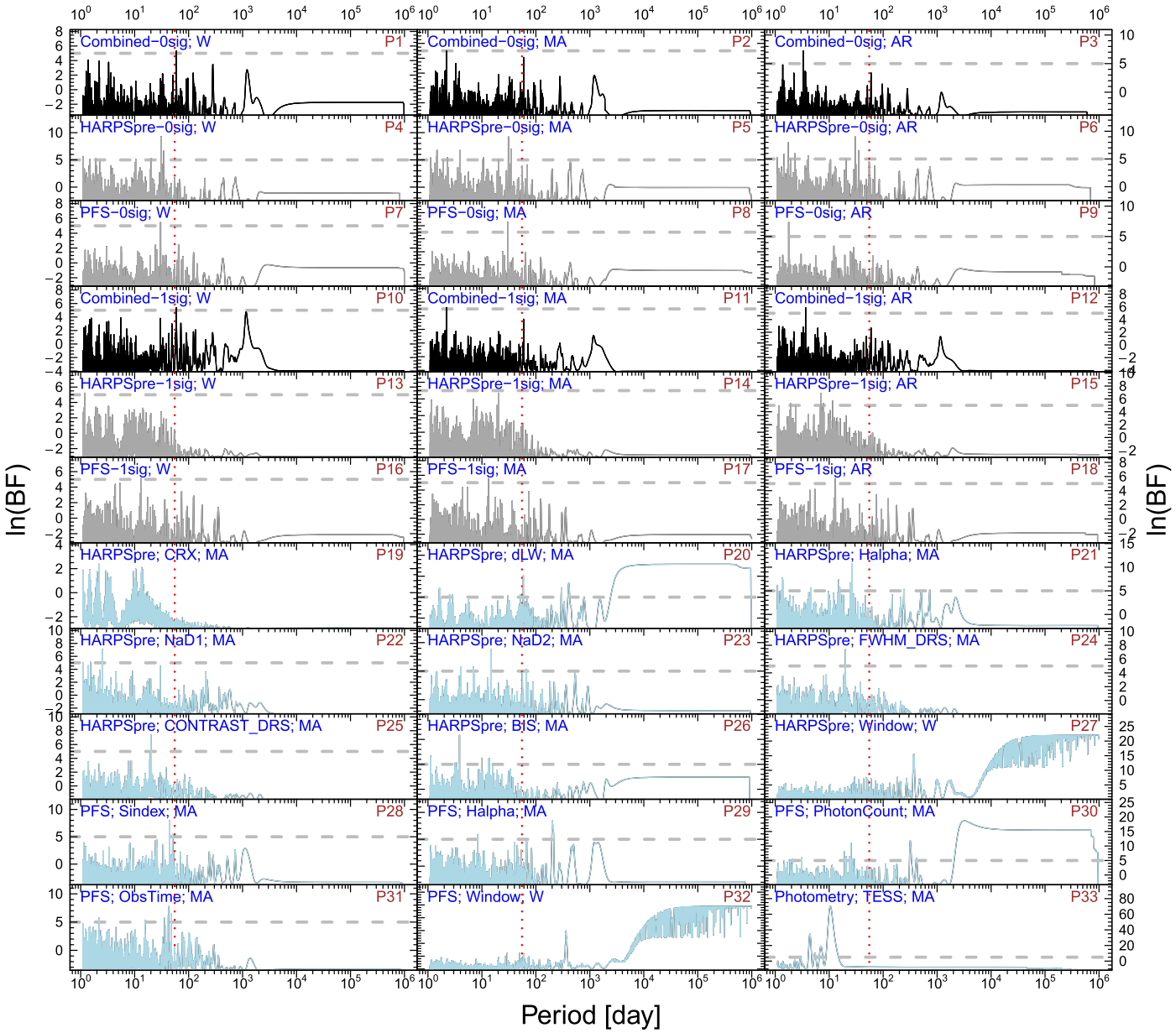

Figure 11. BFPs for the RVs and noise proxies for HIP 107772. The red lines denote the 55.3 day Keplerian signal.

4.2. Individual Planet Candidates

We discuss the results for individual targets by applying the diagnostic criteria introduced in Section 3. The MPs for all of the signals are shown in Figure 5. We will use these MPs as well as the BFPs for the RV data and the corresponding activity indicators as clues for the investigation of the origin of the identified signals.

1. *GJ 2056* (HIP 34785) is an M0-type star with a rotation period of about 32 days (Astudillo-Defru et al. 2017) based on a study of Ca II H and K emission lines. As is seen in Figure 6, a signal at a period of 3000 days can be identified in the BFPs for different noise models (P1–P3) although the phase is not well covered by the data, as shown in Figure 2. The 69.9 day signal corresponds to a planet candidate on an eccentric orbit, leading to a low power in the BFPs that assume zero eccentricity. On the other hand, the 69.9 day signal is unique in the MP (Figure 5) despite low power in the early epochs that are sparsely sampled. The MP is not as useful for the 3000 day signal because its period is comparable with the observational baseline. Considering that the orbital phase, especially the periastron, of this candidate is not well sampled by the RVs (see Figure 2), we regard it as a weak Neptune candidate. We confirm GJ 2056 b as a strong Neptune candidate located in the HZ and its potential moons might be habitable.
2. *GJ 317* (LHS 2037) is an M dwarf with a rotation period of about 69 days according to Astudillo-Defru et al. (2017). Two signals at periods of 692 and >7100 days have been identified by Anglada-Escudé et al. (2012) using Keck data in combination with astrometric data. With HARPS, Keck, and PFS data, we are able to constrain the orbit of GJ 317 b better and identify GJ

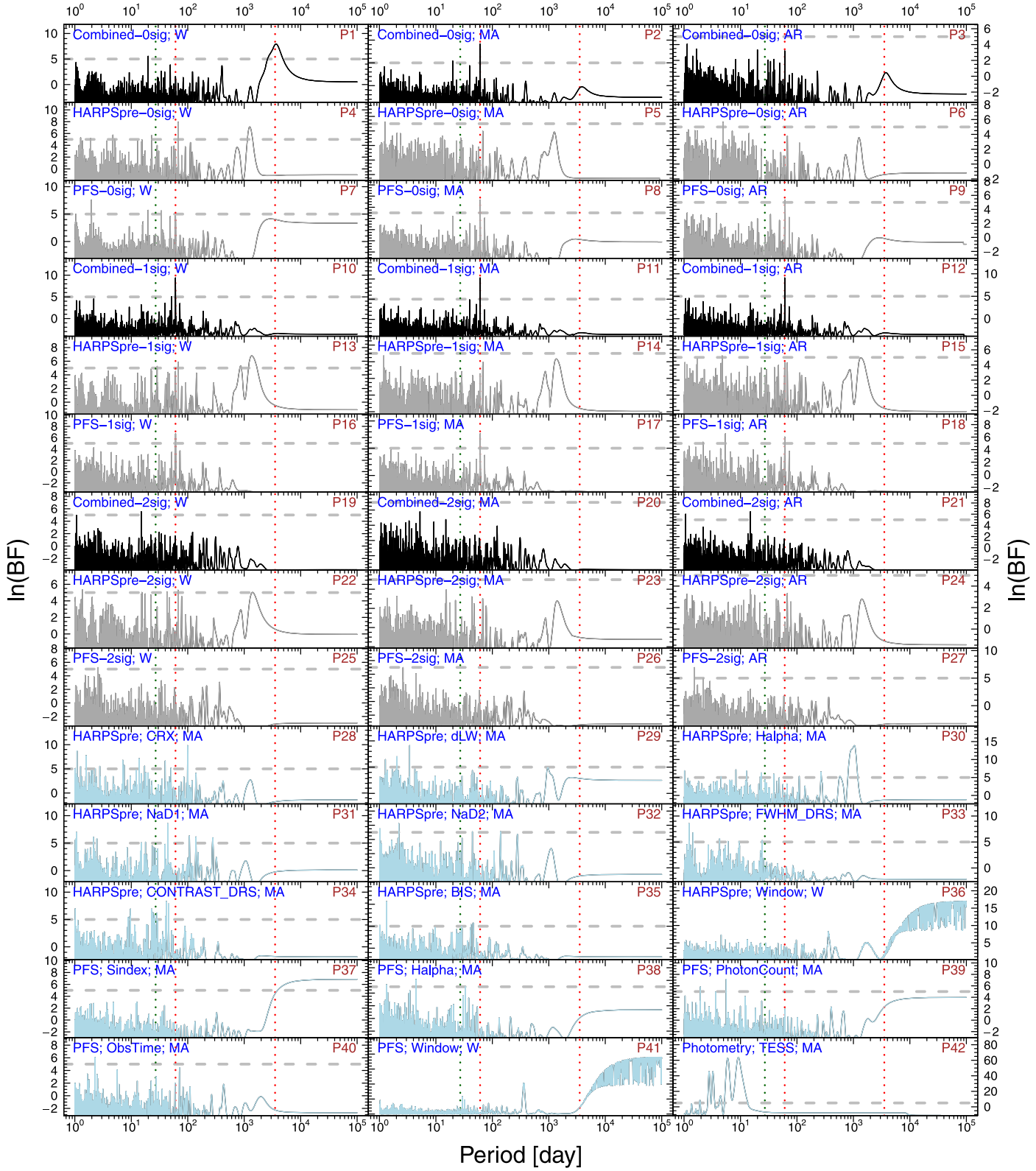

Figure 12. BFPs for the RVs and noise proxies for HIP 38594. The dark green dotted lines denote the literature's 27 day rotation period. The red lines denote the 60.7 and 3525 day Keplerian signals.

317 c as a Jupiter analog with an orbital period of 6700 days and a minimum mass of $2.13 \pm 0.19\,M_{\rm Jup}$. Its semimajor axis is 5.9 ± 0.28 au, similar to the distance from Jupiter to the Sun (5.20 au). Since GJ 317 is only about 15 pc from us, GJ 317 c is about 0.4″ from GJ 317 and thus is detectable by the CGI of WFIRST (Tang et al. 2019). It is evident from the fit to combined set in Figure 2 that these two signals are very significant. This is also demonstrated in the MP shown in Figure 5 and the BFPs in Figure 7.

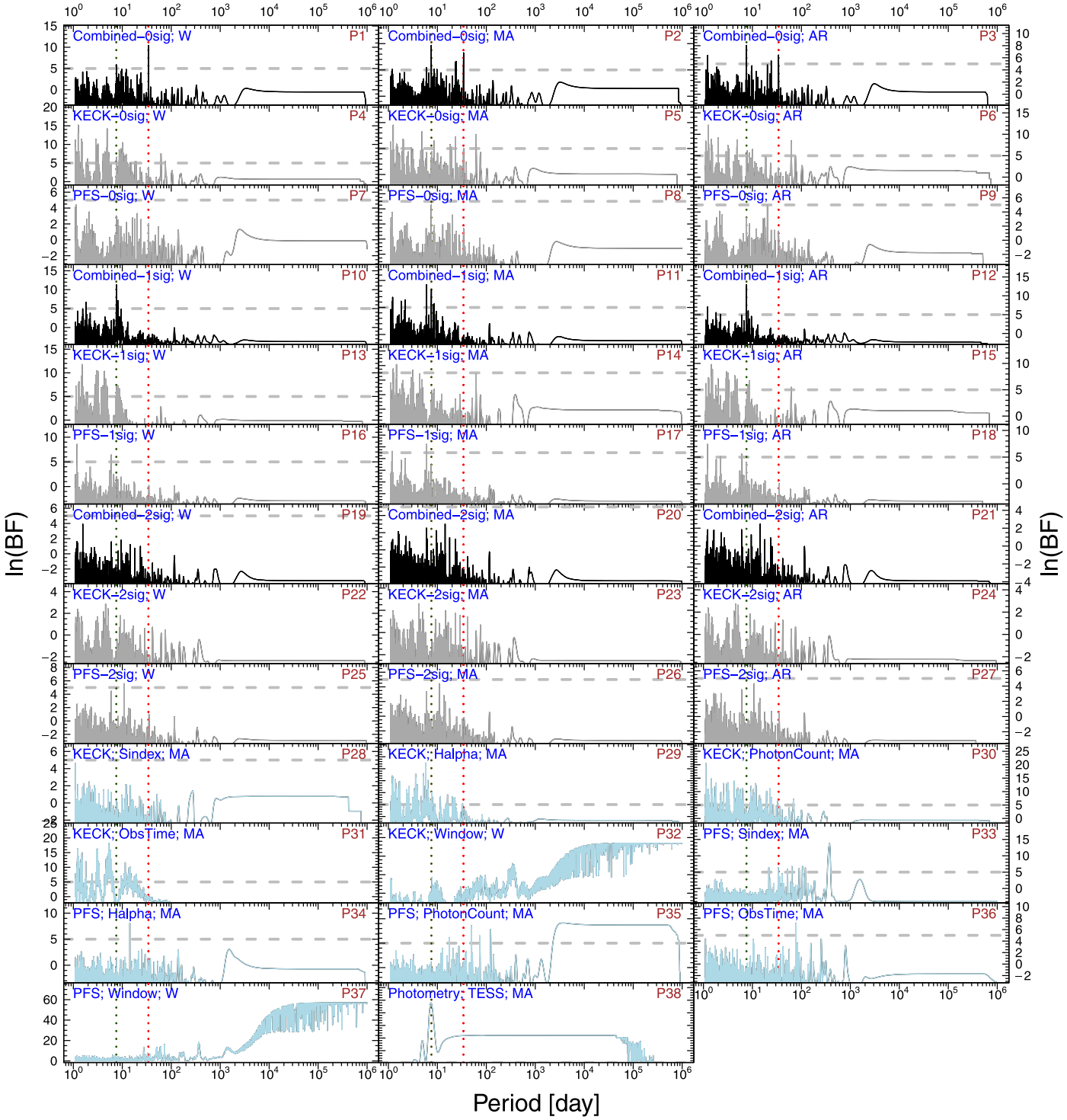

Figure 13. BFPs for the RVs and noise proxies for HIP 4845. The dark green dotted lines denote the 7.6 day rotation period determined in this work. The red lines denote the 34.2 day Keplerian signal.

3. *GJ 480* (Wolf 433 or HIP 61706) is a high proper motion red dwarf. We confirm the detection of this signal with a comprehensive analysis of the combined HARPS and Keck data. The signal is robust to the choice of noise models (P1–P3 in Figure 8) and is consistent over time (Figure 5). We also identify an activity signal at a period of 49.3 ± 0.2 days, which is significant in the BFPs for NaD1 (P22 in Figure 8) and Hα (P21) of the HARPSpre data.

4. *GJ 687* (LHS 450 or HIP 86162) is a red dwarf with a rotation period of about 60 days (Burt et al. 2014). It is found to host at least one planet at a period of 38.14 days (Burt et al. 2014). In our combined analysis of APF, Keck, and SOPHIE, we confirm previous findings and improve the parameter estimation. However, we find a solution with higher eccentricity for the 758 day signal that is probably due to the broader Gaussian prior adopted for eccentricity in this work. This signal is not sensitive to

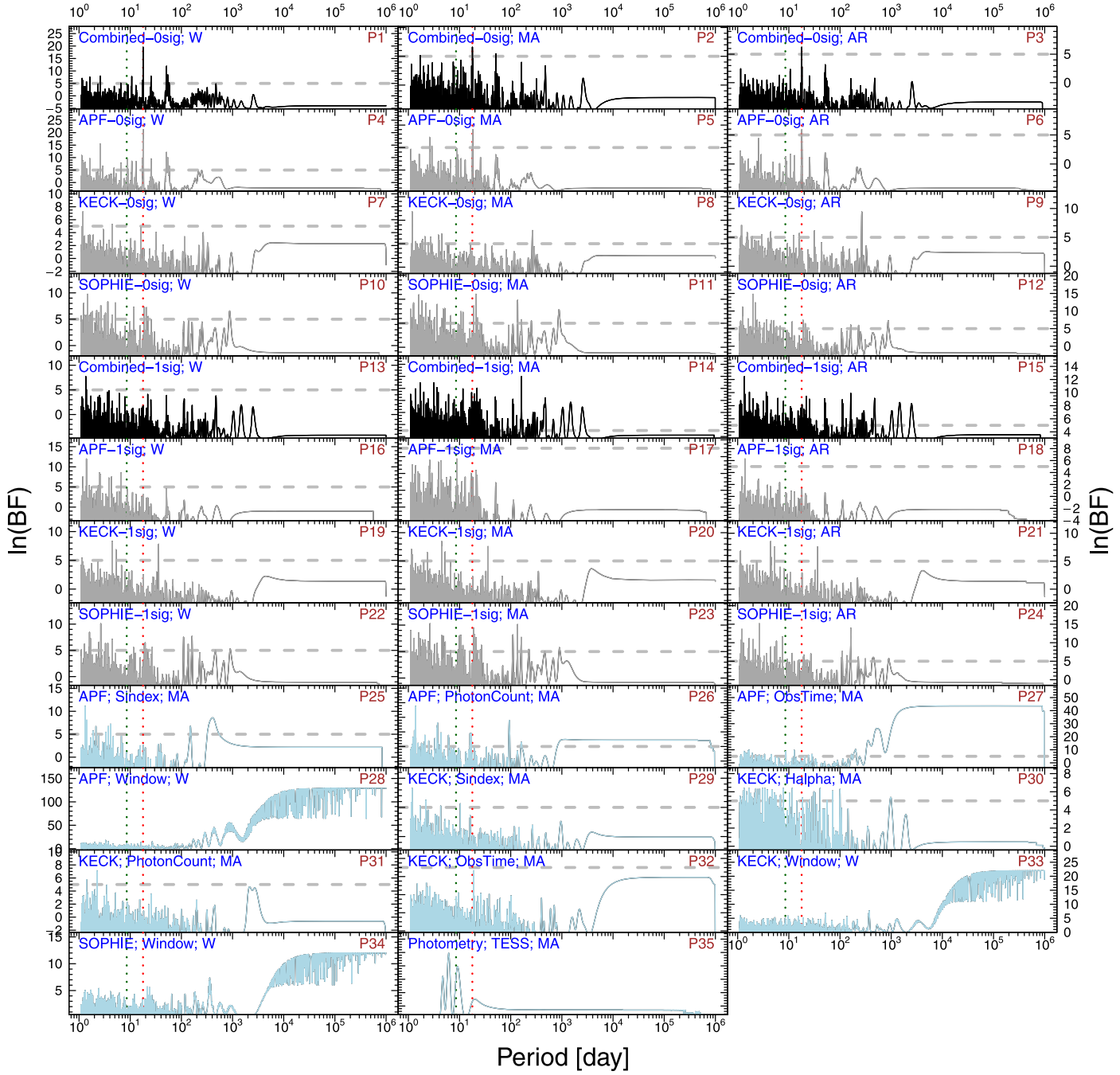

Figure 14. BFPs for the RVs and noise proxies for HIP 48714. The dark green dotted lines denote the literature's 8.55 day rotation period. The red lines denote the 17.8 day Keplerian signal.

the choice of noise models (P1–P3 in Figure 9). The 38.1 days signal is found in both the APF and Keck sets (P4–P9) while the 726 days signal is only found in the Keck set because the APF baseline is too short for such a long period signal (see the raw data in Figure 5). Hence we consider these two signals to be strong planet candidates.

5. *GJ 9066* (LHS 11 or GJ 83.1) is an eruptive variable red dwarf with a rotation period of about 30 days (Astudillo-Defru et al. 2017). Based on our combined analysis of the HARPS and Keck data, we regard the signals at periods of 769 and 242 days as robust planet candidates. The 769 and 242 day signals are significant in the Keck data (P7–P9 and P16–P18 in Figure 10). The 30 day rotation signal is significant in the BFP for Keck S-index (P38). The 242 day signal is quite consistent over time while the 773 day signal is more significant in recent epochs than in previous ones due to recent high cadence sampling (Figure 5). In particular, these two-planet candidates form a 3:1 mean motion resonance, which may stabilize the system over long timescales.
6. *HIP 107772* (TYC 7986-911-1) is a red dwarf without any known planets. A signal around 55 days is found to be significant. This signal fit the RV data well (see Figure 2) and it is consistently significant over time (Figure 5). This signal is identifiable in the BFPs for

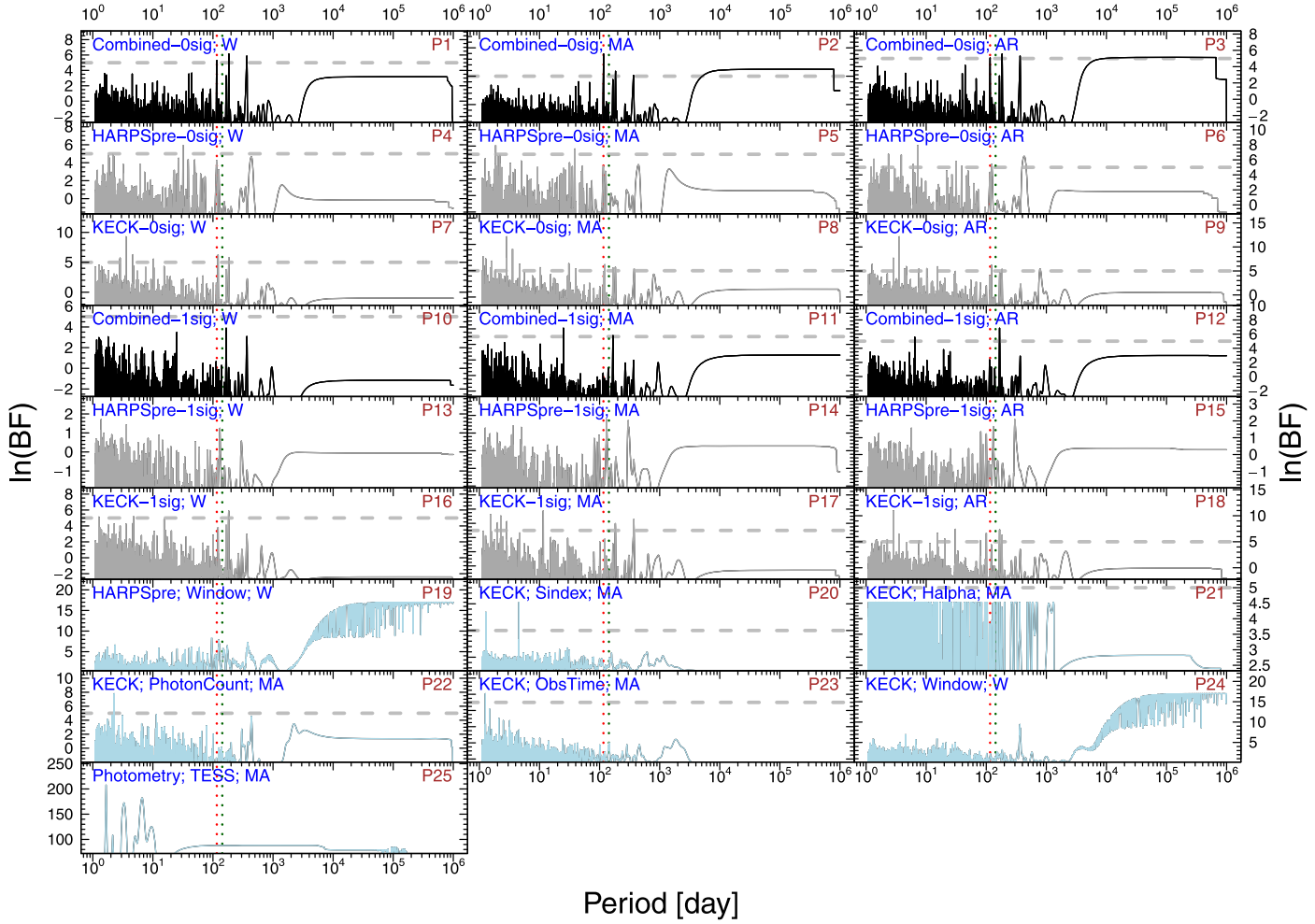

Figure 15. BFPs for the RVs and noise proxies for HIP 60559. The dark green dotted lines denote the literature's 143 day rotation period. The red lines denote the 116 day Keplerian signal.

different noise models (P1–P3 in Figure 11) and different data sets (P2–P9 in Figure 11). It does not overlap with the activity signals (P19–P33 in Figure 11). Hence this signal corresponds to a strong Neptune candidate located in the HZ.

7. *HIP 38594* (Ross 429) is a red dwarf rotating with a period of about 27 days (Astudillo-Defru et al. 2017). Two signals at periods of 60.7 and 3480 days are found to be significant based on the combined analysis of the HARPS and PFS data. The MP shows good time consistency for HIP 38594 b despite cadence-dependent variation in power (Figure 5). However, the period of HIP 38594 c is too long for a time-consistency test although the signal is apparent in the residual RVs (see the panel for HIP 38594 c in Figure 5). In particular, HIP 38594 b is a super-Earth located in the optimistic HZ, as shown in Figure 4. As shown by Figure 12, the two signals are not found to be significant in the BFPs for activity indices. Hence we regard the two signals as strong planet candidates.
8. *HIP 4845* (GJ 3072) is an M dwarf without known planet. Through combined analysis of the HARPS, Keck, and PFS data, we find two signals at periods of 7.6 and 34.2 days. The former is found to be significant in the periodogram for the the Transiting Exoplanet Survey Satellite (TESS) data (P38 of Figure 13) while the later corresponds to a warm super-Earth. The MP for the 34.2 day signal (Figure 5) shows consistent significance over time. This signal is less significant in recent epochs because of low cadence sampling. It is robust to the choice of noise models (P1–P3 and P10–P12 in Figure 13) and is identifiable in the Keck and PFS individual sets (e.g., P5, P8, P14, and P17 in Figure 13). Thus we regard the 34.2 day signal as a strong planet candidate. Although the 7.6 day signal is as significant and as consistent as the 34.2 day signal, it overlaps with the signal found in TESS photometric data, suggesting an activity origin. This demonstrates the importance of a comprehensive diagnostics of activity signals, which are sometimes very similar to Keplerian signals.
9. *HIP 48714* (GJ 373 or LHS 2211) is a red dwarf with a rotation period of 8.55 days (Oelkers et al. 2018). A super-Earth with an orbital period of 17.8 days is found to orbit around the star based on our combined analysis of the APF, Keck, and SOPHIE data. As shown in the MP in Figure 5, the 17.8 day signal is especially significant in recent epochs dominated by high cadence APF data. Since the earlier epochs are not well sampled, such inconsistency is not due to the intrinsic time variability of the signal. As shown in Figure 14, the signal is robust to the choice of noise models (P1–P3). It is significant in the

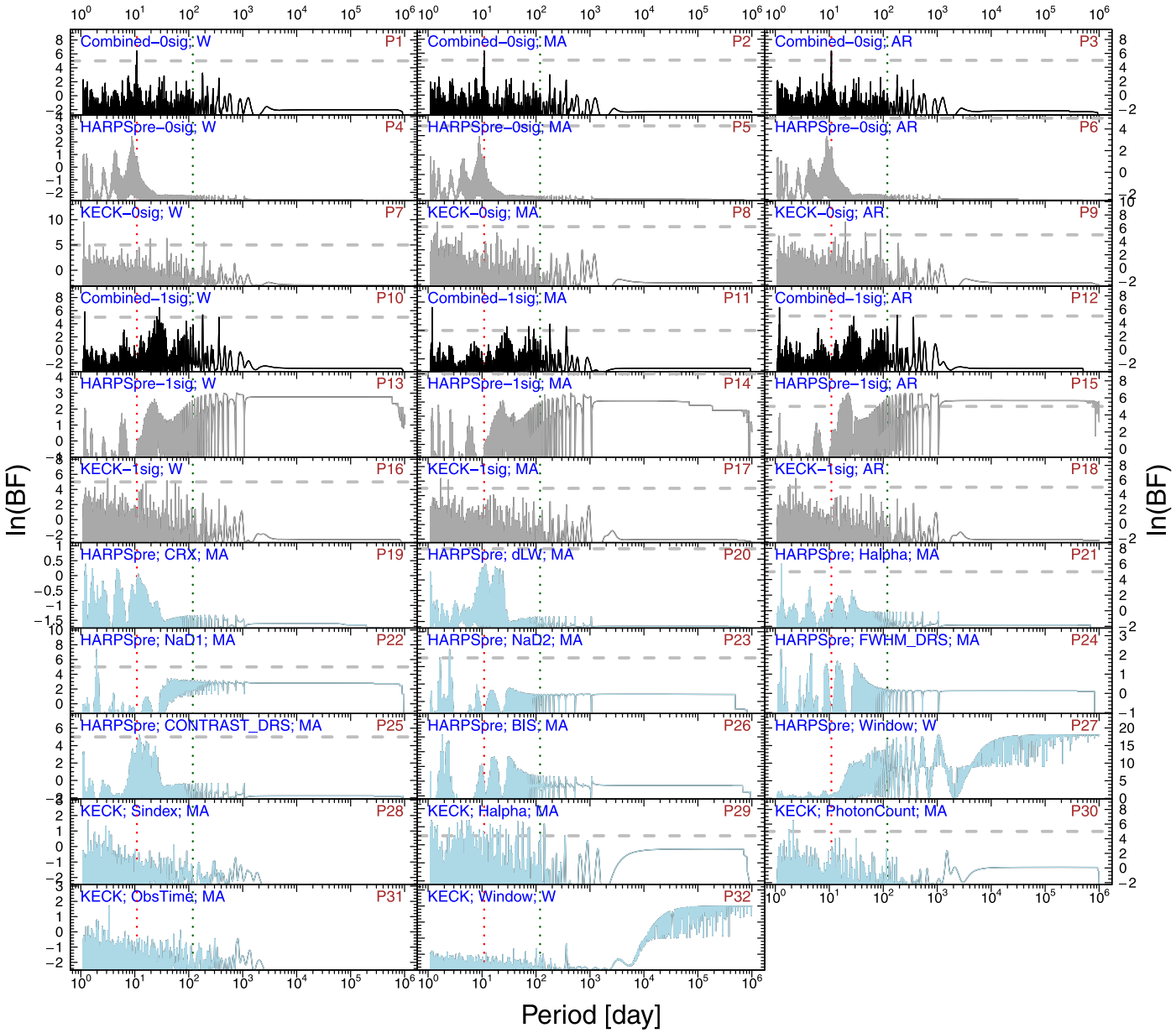

Figure 16. BFPs for the RVs and noise proxies for HIP 67164. The dark green dotted lines denote the literature's 119 day rotation period. The red lines denote the 10.9 day Keplerian signal.

APF set (P4) and is identifiable in the Keck set (P7). The signal does not overlap with activity signals (P25–P35). Therefore we conclude that the 17.8 day signal is a strong super-Earth candidate.

10. *HIP 60559* (Ross 695) is a red dwarf with a rotation period of about 143 days (Astudillo-Defru et al. 2017). A signal at a period of 116 days is identified based on the combined analysis of HARPS and Keck data. The signal is not sensitive to the choice of noise models (P1–P3 in Figure 15) and is identifiable in both the HARPS and Keck data sets. As shown in Figure 5, the period of the 116 day signal seems to vary slightly due to aliasing and low cadence sampling. Thus we consider it to be a weak Neptune candidate.
11. *HIP 67164* (LHS 2794 or GJ 3804) is a red dwarf with a rotation period of about 119 days (Astudillo-Defru et al. 2017). A signal at a period of 10.9 days is identified through the combined analysis of HARPS and Keck data. The signal is robust to the choice of noise models (P1–P3 in Figure 16) and is identifiable in the HARPS (P6) and Keck sets (P7). However, due to the highly irregular sampling of the data, it does not show consistent significance over time in the MP. We consider this signal to be a weak candidate.

5. Dynamical Stability

In the same manner as Paper II, we examine the dynamical stability of the new planet candidates with a large suite of numerical simulations utilizing the *Mercury*6 mixed-variable symplectic integrator (MVS; Chambers 1999). These simulations are designed to quickly identify unstable regions of parameter space within our calculated uncertainties for the planets' orbital elements (Table 3). Thus, while a definitive proof of each systems' stability is beyond the scope of this work, systems that evolve regularly in each of our various

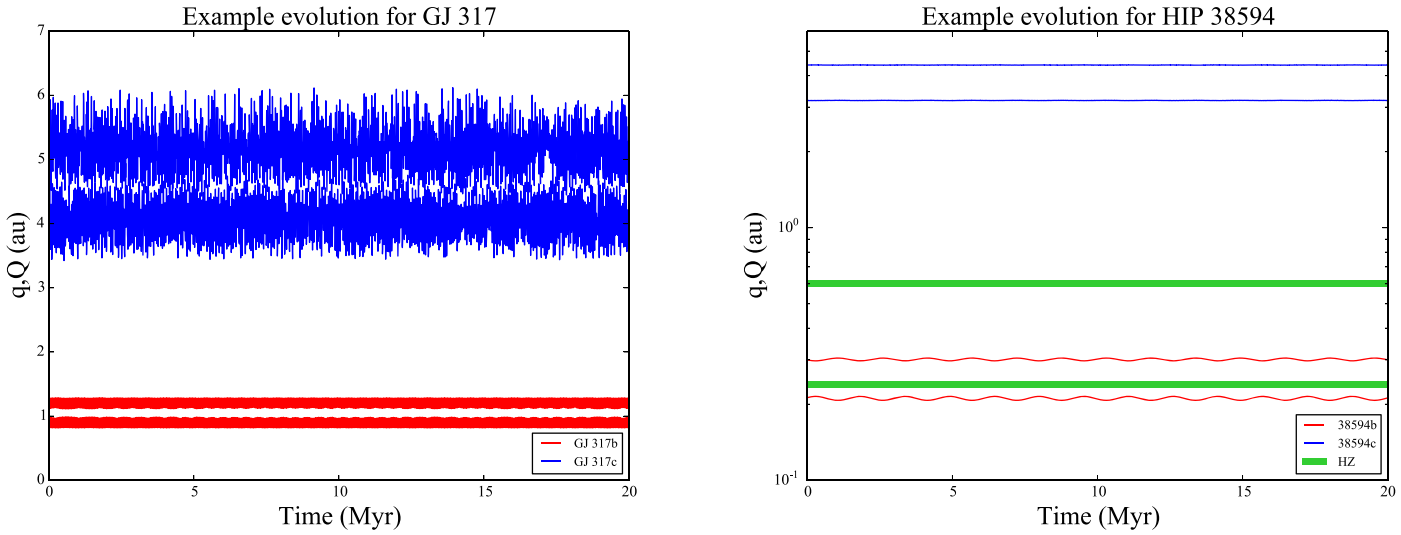

Figure 17. Example evolutionary scheme from two of our dynamical simulations studying the GJ 317 and HIP 38594 systems. The pericenter and apocenter for each planet are respectively plotted with blue (GJ 317 c and HIP 38594 c) and red (GJ 317 b and HIP 38594 b) lines. The inner and outer edges of the HZ of HIP 38594are shown by horizontal green lines.

realizations are highly likely to be stable (though we do not consider possible perturbations from additional, undetected planets).

For each multi-planet system we consider a grid of five eccentricities and masses for each object within the ranges of uncertainties for the respective parameters reported in Table 3. As in Paper II, we also analyze three possible orientations for each planetary system: $I = 30°$, 60°, and 90°. Thus, each individual system is scrutinized with 1875 separate numerical simulations. Planetary inclinations are selected randomly from nearly co-planar distributions, and the remaining angular orbital elements (i.e., those not listed in Table 3) are selected at random from uniform distributions. Each system is integrated for 1 Myr utilizing a time step equal to ∼5% of the inner planet's orbital period (e.g.: Gilbert et al. 2020). Systems containing at least one planet with $e > 0.5$ are integrated for 20 Myr to account for high-eccentricity dynamics. The results of our dynamical analysis are summarized as follows:

1. *Systems exhibiting regular behavior.* Within our tested parameter space, the two-planet systems GJ 2056, GJ 317, GJ 9066, and HIP 38594 display no evidence of instability or chaotic evolution (e.g., Laskar 1997). In all cases, the planets' orbits are governed by regular secular oscillations in e, the magnitude of which are related to their masses and initial eccentricities (e.g., Murray & Dermott 1999). The largest such oscillations occur in GJ 317, the system possessing the most massive planets. An example of the evolution of this system is plotted in the left panel of Figure 17. As GJ 317 b and c are well separated in terms of their orbital period ratio for all of our tested combinations of semimajor axes ($P_c/P_b \sim 10$), our simulations suggest that this system is dynamically stable.
2. *Dynamical stability of HIP 38594.* We also study the dynamical stability of HIP 38594, the host of an HZ super-Earth. As shown in the right panel of Figure 17, HIP 38594 b migrates into and out of the HZ when approaching its apocenter and pericenter, respectively. However, such a noncircular orbit might not be representative because the eccentricity given in Table 3 is consistent with zero at the 2σ confidence level. Assuming a circular orbit, HIP 38594 b would be stable over at least a few million years in the HZ.
3. *System with unstable parameter space: GJ 687.* In 5% of our simulations investigating the stability of GJ 687, the inner planets' pericenter was excited to the point that the planet collided with the central body. This occurred exclusively in our integrations testing the largest eccentricities (≃0.62) and masses ($M \gtrsim 36\,M_\oplus$ for the $I = 30°$ case) for the outer planet. In these isolated instances, the planets begin on nearly-crossing orbits where they interact strongly with each other. The more massive outer planet's eccentric forcing on GJ 687 b drives large secular oscillations in the smaller planet's eccentricity, eventually driving its pericenter on to a collision course with the central star. As the average timescale for the loss of GJ 687 b in our simulations (∼300 Kyr) is significantly less than the system's age, and the planets evolve regularly within the remainder of our tested parameter space, we conclude that the system is indeed stable. Thus, our results imply additional constraints on the eccentricity and mass of GJ 687 c, likely limiting them to the lower range of the values reported in Table 3 (specifically, $e \lesssim 0.51$ for nominal mass values and $e \lesssim 0.40$ for $M_c \gtrsim 36\,M_\oplus$).

6. Discussion and Conclusion

In this work, we identify 10 strong planet candidates as well as three weak candidates, and confirm three previous candidates. Weak candidates need followup investigations to confirm. The strong planet candidates satisfy the planet selection criteria and are unlikely to be caused by stellar activity based on our diagnostics. We also confirm previous candidates and improve their orbital solutions through our independent analyses. Among these planet candidates, there are one temperate super-Earth, four hot super-Earths, three temperate Neptunes, four cold Neptunes, and four cold Jupiters.

To date, HIP 38594 is the most massive M-dwarf host of temperate Earths and super-Earths that are found through the RV method. As an early-type M dwarf, HIP 38594 is a Goldilocks M-dwarf host for habitable planets because it is less active and has a larger HZ than other types of M dwarfs. We also investigate the dynamical stability of the HZ planet, HIP 38594 b, and find that the orbit of the planet partially overlaps with the HZ. Considering that the orbital solution for this planet is consistent with a circular orbit, HIP 38594 b is probably on a nearly circular orbit and is thus unlikely to migrate out of the HZ frequently.

We also detect three temperate Neptunes and four cold Neptunes, contributing significantly to a rarely explored population. On the other hand, we find four cold Jupiters, equal to the number of cold Neptunes. Considering the fact that cold Jupiters induce larger RV semi-amplitudes and are thus easier to detect, the sample of cold Neptunes and Jupiters detected in this work are consistent with a high occurrence rate of cold Neptunes inferred from microlensing observations by Suzuki et al. (2016, p. 1). They conclude that "cold Neptunes are likely to be the most common type of planets beyond the snow line." Cold Neptunes have rarely been detected through the RV method until the recent accumulation of large amount of RV data. Due to their relatively large angular separation from their hosts, the cold Neptunes and cold Jupiters detected in this work are good targets for direct imaging by future facilities such as HabEx and ELT.

Our discovery of multiple planets in RV data demonstrates the feasibility of a comprehensive RV survey of nearby planets, especially Earth analogs. Based on combined analyses of all available RV data for M dwarfs, we are able to select the most promising targets for further analyses and followup observations. This leads to the identification of smaller planets embedded in noisy RV time series obtained by different groups. Our stellar activity diagnostics allow us to classify signals into different categories by accounting for their consistency over time, robustness to the choice of noise models, and overlaps with activity signals. In particular, the MPs visualize the time consistency of signals, and the BFPs test the sensitivity of signal-to-noise models and stellar activity. Nevertheless, stellar activity is still the major challenge to the detection of smaller signals caused by Earth twins. According to our analyses of the RV data for nearby M dwarfs in Paper II and this paper, stellar variability sets the current limit of detectable RV signals for M dwarfs to be $\sim 1\,\mathrm{m\,s^{-1}}$. Our detection of temperate super-Earths and cold Neptunes around early-type M dwarfs slightly above this limit suggest a large undetected population of small planets embedded in the current RV data.

This work has made use of data from the European Space Agency (ESA) mission Gaia (https://www.cosmos.esa.int/gaia), processed by the Gaia Data Processing and Analysis Consortium (DPAC, https://www.cosmos.esa.int/web/gaia/dpac/consortium). Funding for the DPAC has been provided by national institutions, in particular the institutions participating in the Gaia Multilateral Agreement. This research has also made use of the Keck Observatory Archive (KOA), which is operated by the W. M. Keck Observatory and the NASA Exoplanet Science Institute (NExScI), under contract with the National Aeronautics and Space Administration. This research has also made use of the services of the ESO Science Archive Facility, NASA's Astrophysics Data System Bibliographic Service, and the SIMBAD database, operated at CDS, Strasbourg, France. Support for this work was provided by NASA through Hubble Fellowship grant HST-HF2-51399.001 awarded by the Space Telescope Science Institute, which is operated by the Association of Universities for Research in Astronomy, Inc., for NASA, under contract NAS5-26555. The authors acknowledge the years of technical support from LCO staff in the successful operation of PFS, enabling the collection of the data presented in this paper. We would also like to acknowledge the many years of technical support from the UCO/Lick staff for the commissioning and operation of the APF facility atop Mt. Hamilton. Part of this research was carried out at the Jet Propulsion Laboratory, California Institute of Technology, under a contract with the National Aeronautics and Space Administration (NASA).

Software: R package magicaxis (Robotham 2016), fields (Nychka et al. 2018), MASS (Venables & Ripley 2002), minpack.lm (Elzhov et al. 2016).

ORCID iDs

Fabo Feng https://orcid.org/0000-0001-6039-0555
Matthew S. Clement https://orcid.org/0000-0001-8933-6878
Steven S. Vogt https://orcid.org/0000-0001-7177-7456
Jennifer Burt https://orcid.org/0000-0002-0040-6815
Jeffrey D. Crane https://orcid.org/0000-0002-5226-787X
Bradford Holden https://orcid.org/0000-0002-6153-3076
Matías R. Díaz https://orcid.org/0000-0002-2100-3257
R. Paul Butler https://orcid.org/0000-0003-1305-3761

References

Anglada-Escudé, G., Amado, P. J., Barnes, J., et al. 2016, Natur, 536, 437
Anglada-Escudé, G., Boss, A. P., Weinberger, A. J., et al. 2012, ApJ, 746, 37
Artigau, É, Kouach, D., Donati, J.-F., et al. 2014, Proc. SPIE, 9147, 914715
Astudillo-Defru, N., Delfosse, X., Bonfils, X., et al. 2017, A&A, 600, A13
Bechter, A. J., Bechter, E. B., Crepp, J. R., Jr, King, D., & Crass, J. 2018, Proc. SPIE, 10702, 107026T
Bryan, M. L., Knutson, H. A., Lee, E. J., et al. 2019, AJ, 157, 52
Burt, J., Vogt, S. S., Butler, R. P., et al. 2014, ApJ, 789, 114
Butler, R. P., Marcy, G. W., Williams, E., et al. 1996, PASP, 108, 500
Butler, R. P., Vogt, S. S., Laughlin, G., et al. 2017, AJ, 153, 208
Butler, R. P., Wright, J. T., Marcy, G. W., et al. 2006, ApJ, 646, 505
Chambers, J. E. 1999, MNRAS, 304, 793
Courcol, B., Bouchy, F., Pepe, F., et al. 2015, A&A, 581, A38
Crane, J. D., Shectman, S. A., & Butler, R. P. 2006, Proc. SPIE, 6269, 626931
Crane, J. D., Shectman, S. A., Butler, R. P., et al. 2010, Proc. SPIE, 7735, 773553
Crane, J. D., Shectman, S. A., Butler, R. P., Thompson, I. B., & Burley, G. S. 2008, Proc. SPIE, 7014, 701479
Cuntz, M., & Guinan, E. F. 2016, ApJ, 827, 79
Danielski, C., Baudino, J.-L., Lagage, P.-O., et al. 2018, AJ, 156, 276
Dumusque, X., Boisse, I., & Santos, N. 2014, ApJ, 796, 132
Dumusque, X., Borsa, F., Damasso, M., et al. 2017, A&A, 598, A133
Elzhov, T. V., Mullen, K. M., Spiess, A.-N., et al. 2016, Title R Interface to the Levenberg-Marquardt Nonlinear Least-Squares Algorithm Found in MINPACK, Plus Support for Bounds, https://cran. rproject. org/web/packages/minpack. lm/minpack. lm. pdf
Feng, F., Butler, R. P., Shectman, S. A., et al. 2020, ApJS, 246, 11
Feng, F., Crane, J. D., Xuesong Wang, S., et al. 2019, ApJS, 242, 25
Feng, F., Lisogorskyi, M., Jones, H. R. A., et al. 2019, ApJS, 244, 39
Feng, F., Tuomi, M., & Jones, H. R. A. 2017a, MNRAS, 470, 4794
Feng, F., Tuomi, M., Jones, H. R. A., et al. 2017b, AJ, 154, 135
Feng, F., Tuomi, M., Jones, H. R. A., Butler, R. P., & Vogt, S. 2016, MNRAS, 461, 2440
Fischer, D., Anglada-Escude, G., Arriagada, P., et al. 2016, PASP, 128, 066001
Gaudi, B. S., Seager, S., Mennesson, B., et al. 2020, arXiv:2001.06683.

Gilbert, E. A., Barclay, T., Schlieder, J. E., et al. 2020, AJ, 160, 116
Gillon, M., Triaud, A. H. M. J., Demory, B.-O., et al. 2017, Natur, 542, 456
Haario, H., Saksman, E., & Tamminen, J. 2001, Bernoulli, 7, 223
Halverson, S., Terrien, R., Mahadevan, S., et al. 2016, Proc. SPIE, 9908, 99086P
Heller, R., & Armstrong, J. 2014, AsBio, 14, 50
Jordi, C., Gebran, M., Carrasco, J. M., et al. 2010, A&A, 523, A48
Jurgenson, C., Fischer, D., McCracken, T., et al. 2016, Proc. SPIE, 9908, 99086T
Kane, S. R., Ciardi, D. R., Gelino, D. M., & von Braun, K. 2012, MNRAS, 425, 757
Kass, R. E., & Raftery, A. E. 1995, J. Am. Stat. Assoc., 90, 773
Kay, C., Opher, M., & Kornbleuth, M. 2016, ApJ, 826, 195
Kopparapu, R. K., Ramirez, R. M., SchottelKotte, J., et al. 2014, ApJL, 787, L29
Laskar, J. 1997, A&A, 317, L75
Levenberg, K. 1944, QApMa, 2, 164
Lomb, N. R. 1976, Ap&SS, 39, 447
Mahadevan, S., Ramsey, L., Bender, C., et al. 2012, Proc. SPIE, 8446, 84461S
Marquardt, D. W. 1963, SIAM J., 11, 431
Mohanty, S., & Basri, G. 2003, ApJ, 583, 451
Murray, C. D., & Dermott, S. F. 1999, Solar System Dynamics (Cambridge: Cambridge Univ. Press)
Nychka, D., Furrer, R., Paige, J., Sain, S., & Nychka, M. D. 2018, fields: Tools for spatial data v11.4, GitHub, doi:10.5065/D6W957CT
Oelkers, R. J., Rodriguez, J. E., Stassun, K. G., et al. 2018, AJ, 155, 39
Pepe, F., Mayor, M., Rupprecht, G., et al. 2002, Msngr, 110, 9
Pepe, F. A., Cristiani, S., Rebolo Lopez, R., et al. 2010, Proc. SPIE, 7735, 77350F
Perrot, C., Baudoz, P., Boccaletti, A., et al. 2018, arXiv:1804.01371
Perruchot, S., Kohler, D., Bouchy, F., et al. 2008, Proc. SPIE, 7014, 70140J
Perryman, M., Hartman, J., Bakos, G. Á, & Lindegren, L. 2014, ApJ, 797, 14
Quirrenbach, A., Amado, P. J., Mandel, H., et al. 2010, in ASP Conf. Ser. 430, Pathways Toward Habitable Planets, ed. V. Coudé du Foresto, D. M. Gelino, & I. Ribas (San Francisco, CA: ASP), 521
Ribas, I., Tuomi, M., Reiners, A., et al. 2018, Nat., 563, 365
Robotham, A. S. G. 2016, Magicaxis: Pretty Scientific Plotting with Minor-tick and log Minor-tick Support, Astrophysics Source Code Library, ascl:1604.004
Scargle, J. D. 1982, ApJ, 263, 835
Schwab, C., Rakich, A., Gong, Q., et al. 2016, Proc. SPIE, 9908, 99087H
Shields, A. L., Ballard, S., & Johnson, J. A. 2016, PhR, 663, 1
Soubiran, C., Jasniewicz, G., Chemin, L., et al. 2018, A&A, 616, A7
Spiegelhalter, D. J., Best, N. G., Carlin, B. P., & Van Der Linde, A. 2002, J. Royal Stat. Soc. Ser. B, 64, 583
Stassun, K. G., Oelkers, R. J., Paegert, M., et al. 2019, AJ, 158, 138
Suzuki, D., Bennett, D. P., Sumi, T., et al. 2016, ApJ, 833, 145
Tal-Or, L., Trifonov, T., Zucker, S., Mazeh, T., & Zechmeister, M. 2019, MNRAS, 484, L8
Tamura, M., Suto, H., Nishikawa, J., et al. 2012, Proc. SPIE, 8446, 84461T
Tang, H., Rodgers, M., Creager, B., et al. 2019, Proc. SPIE, 11117, 111170C
Tarter, J. C., Backus, P. R., Mancinelli, R. L., et al. 2007, AsBio, 7, 30
Trifonov, T., Tal-Or, L., Zechmeister, M., et al. 2020, A&A, 636, A74
Tuomi, M., & Anglada-Escudé, G. 2013, A&A, 556, A111
Van Eylen, V., Albrecht, S., Huang, X., et al. 2019, AJ, 157, 61
Venables, W. N., & Ripley, B. D. 2002, Modern Applied Statistics with S (4th ed.; New York: Springer)
Vogt, S. S., Allen, S. L., Bigelow, B. C., et al. 1994, Proc. SPIE, 2198, 362
Vogt, S. S., Radovan, M., Kibrick, R., et al. 2014, PASP, 126, 359
Wenger, M., Ochsenbein, F., Egret, D., et al. 2000, A&AS, 143, 9
West, A. A., Weisenburger, K. L., Irwin, J., et al. 2015, ApJ, 812, 3
Wright, J., & Eastman, J. 2014, PASP, 126, 838
Zechmeister, M., Dreizler, S., Ribas, I., et al. 2019, A&A, 627, A49
Zechmeister, M., Reiners, A., Amado, P. J., et al. 2018, A&A, 609, A12
Zhu, W., & Wu, Y. 2018, AJ, 156, 92